Edmundo Rafael de Andrade Sérgio

ANÁLISE DA PROPAGAÇÃO DE FENDAS POR FADIGA UTILIZANDO O MODELO DE DANO GTN

Dissertação no âmbito do Mestrado Integrado em Engenharia Mecânica, na especialidade de Produção e Projeto, orientada pelo Professor Doutor Diogo Mariano Simões Neto e pelo Mestre Micael Frias Borges e apresentada ao Departamento de Engenharia Mecânica da Faculdade de Ciências e Tecnologia da Universidade de Coimbra

Julho de 2021

1290

FACULDADE DE CIÊNCIAS E TECNOLOGIA
UNIVERSIDADE DE COIMBRA

Fatigue crack propagation analysis using the GTN damage model

Submitted in Partial Fulfilment of the Requirements for the Degree of Master's in Mechanical Engineering in the speciality of Production and Project.

Análise da propagação de fendas por fadiga utilizando o modelo de dano GTN

Author
Edmundo Rafael de Andrade Sérgio

Advisors
Micael Frias Borges
Diogo Mariano Simões Neto

Jury

President	**Professor Doutor Luís Filipe Martins Meneses** **Professor Catedrático da Universidade de Coimbra**
Vowel	**Professor Doutor José Luís Carvalho Martins Alves** **Professor Associado da Universidade do Minho**
Advisor	**Professor Doutor Diogo Mariano Simões Neto** **Professor Auxiliar da Universidade de Coimbra**

Coimbra, July, 2021

If I have seen further, it is by standing upon the shoulders of giants

Isaac Newton, 1675

ACKNOWLEDGEMENTS

This work was carried out under the project “IfDamagElse: Modelling and numerical simulation of damage in metallic sheets: anisotropic behaviour and tension-compression asymmetry coupled approach for formability prediction” (PTDC/EME-EME/30592/2017) and “Sim2AM: Computational Methods for Optimizing the SLM Additive Manufacturing Process” (PTDC/EME-EME/31657/2017) co-funded by the Foundation for Science and Technology and the EU/FEDER, through the program COMPETE 2020 (POCI-01-0145-FEDER-030592, CENTRO-01-0145-FEDER-031657 and UIDB/00285/2020).

Abstract

Fatigue is one of the most prominent mechanisms of failure. Thus, its evaluation is of prime order in engineering components subjected to cyclic loads. The fatigue crack growth process is usually accessed through the stress intensity factor, *ΔK*. In accordance, the fatigue crack growth rate is, typically, defined by the *da/dN*- *ΔK* curves. Despite the wide use of this approach, it has some well-known limitations. Moreover, the fatigue process is an irreversible mechanism while the *ΔK* parameter is of elastic nature.

The cumulative plastic strain at the crack tip has provided results in good agreement with the experimental observations, appearing as an alternative to the more traditional *ΔK* approach. Also, it allows understanding the crack tip phenomena leading to FCG. Plastic deformation inevitably leads to micro-porosity occurrence and damage accumulation, which can be evaluated with a damage model, such as Gurson-Tvergaard-Needleman (GTN).

In this study a numerical model that uses the cyclic plastic strain at the crack tip to predict da/dN was coupled with the GTN damage model. The crack propagation process occurs, by node release, when the cumulative plastic strain reaches a critical value. The GTN model is used to account for the material degradation due to the growth of micro-voids process, which affects fatigue crack growth. Crack propagation predictions, of the 2024-T351 aluminium alloy, with GTN are compared with the ones obtained without the ductile fracture model. The accuracy of both models is evaluated through the comparison with experimental fatigue test results from CT specimens. The influence of the GTN parameters, related to growth and nucleation of micro-voids, on the predicted crack growth rate is, also, accessed.

Keywords: Fatigue crack growth, Crack tip plastic deformation, GTN damage model, Sensitivity analysis

Resumo

A fadiga dos materiais é um dos mais principais mecanismos de falha em componentes mecânicos. Assim, a sua avaliação é essencial nos componentes de engenharia sujeitos a cargas cíclicas. O processo de propagação de fendas por fadiga é normalmente avaliado através da gama do factor de intensidade de tensão, ΔK. Deste modo, a velocidade de propagação de uma fenda é tipicamente definida através das curvas da/dN-ΔK. Apesar da ampla utilização desta abordagem, estão-lhe associadas várias limitações. Além disso, o processo de fadiga é um mecanismo irreversível enquanto o parâmetro ΔK é de natureza elástica.

A utilização da deformação plástica acumulada na ponta da fenda provou fornecer resultados em concordância com as observações experimentais, aparecendo como uma alternativa à abordagem mais tradicional baseada no ΔK. Além disso, permite compreender o fenómeno da ponta da fenda que conduz à propagação de fendas por fadiga. A deformação plástica conduz inevitavelmente à ocorrência de micro-vazios e acumulação de dano, que podem ser avaliados com um modelo de dano, como por exemplo o modelo Gurson-Tvergaard-Needleman (GTN).

Neste estudo, o modelo numérico que utiliza a deformação plástica cíclica na extremidade da fenda para prever da/dN foi acoplado com o modelo de dano GTN. O processo de propagação da fenda ocorre, por libertação de nós, quando a deformação plástica cumulativa atinge um valor crítico. O modelo GTN é utilizado para contabilizar a degradação da resistência mecânica do material devido aos processos de crescimento de micro-vazios, que afecta o crescimento da fenda de fadiga. Neste trabalho são feitas previsões de propagação de fendas na liga de alumínio 2024-T351, utilizando o modelo GTN, as quais são comparadas com as obtidas sem o modelo de fratura dúctil. A precisão de ambos os modelos é avaliada através da comparação com resultados de ensaios experimentais em provetes C(T). É também avaliada a influência dos parâmetros do modelo GTN na velocidade de propagação de fendas por fadiga, os quais estão relacionados com o crescimento e nucleação dos micro-vazios.

Palavras-chave: Propagação de fendas por fadiga, Deformação plástica cumulativa na extremidade da fenda, Modelo de dano GTN, Análise de sensibilidade

Contents

LIST OF FIGURES ix

LIST OF TABLES xii

LIST OF SIMBOLS AND ACRONYMS/ ABBREVIATIONS xiv
  List of Symbols xiv
  Acronyms/Abbreviations xvi

1. INTRODUCTION 1

2. LITERATURE REVIEW 3
  2.1. Fatigue Phenomenon 3
  2.2. Linear Elastic Fracture Mechanics 3
    2.2.1. Crack Closure effect on LEFM 5
  2.3. Elasto-plastic Fracture Mechanics 6
    2.3.1. Crack Tip Opening Displacement 7
    2.3.2. Crack Tip Plastic Strain 8
  2.4. Other mechanisms affecting FCG 9
  2.5. Physical mechanisms of the ductile fracture 10
  2.6. A Brief Background on Damage Models 11

3. GTN DAMAGE MODEL 13
  3.1. Calibration of the GTN model parameters 15
  3.2. Applications and modifications to the classical GTN model 16

4. NUMERICAL MODEL 17
  4.1. Material Constitutive Model 17
  4.2. Boundary Conditions and Geometry 18
  4.3. Specimen Discretization 19
  4.4. Loading Case 19
  4.5. Crack Propagation Scheme 20
  4.6. Crack Growth Criteria 21

5. NUMERICAL RESULTS AND DISCUSSION 22
  5.1. FCG modelling with and without GTN 22
    5.1.1. Fatigue Crack Growth Rate 22
    5.1.2. Cumulative Plastic Strain 23
    5.1.3. Size of the Plastic Zone at the Crack Tip 25
    5.1.4. Plasticity Induced Crack Closure 26
    5.1.5. Comparison with Experimental Data 30
  5.2. Porosity, Plastic Strain and Stress Tri-axiality Relation 31
  5.3. Influence of Each GTN Parameter on FCG 34
    5.3.1. Effect of Initial Void Volume Fraction, f_0 34
    5.3.2. Effect of the Tvergaard Parameters, q_1, q_2 and q_3. 38
    5.3.3. Effect of the Void Fraction to be Nucleated, f_N 43
    5.3.4. Effect of the Mean Nucleation Strain, ε_N 46

    5.3.5. Influence of the Standard Deviation, s_N 47
  5.4. Sensitivity Analysis 50

6. CONCLUSIONS 52

7. SUGESTIONS FOR FUTURE WORK 54

BIBLIOGRAPHY 55

LIST OF FIGURES

Figure 2.1 Fatigue crack growth curve. Log-log scale. Adapted from [33]. 5

Figure 2.2. Schematic diagram of crack tip zones. 7

Figure 4.1. Geometry and main dimensions (in mm) of the Compact tension specimen used in the study of the AA2024-T351. [17]. 18

Figure 4.2. Finite element mesh of the CT specimen. The refined mesh is shown in the image on the bottom left corner. Adapted from [20]. 19

Figure 5.1. da/dN-ΔK curves in log-log scale (plane strain; $R = 0.1$; $f_0 = 0.01$; $q_1 = 1.5$; $q_2 = 1$ and $q_3 = 2.25$, nucleation and coalescence are disabled). The Paris-Erdogan law parameters are shown on the equations related to the trend-lines. 23

Figure 5.2. Comparison of the plastic strain evolution with and without GTN for a_0=11.5 mm. (a) time period between the 25th and the 26th node releases; (b) a single load cycle, immediately before the 26th propagation. 24

Figure 5.3. Comparison of the plastic strain evolution with and without GTN for a_0=21.5 mm. (a) time period between the 36th and the 37th node releases; (b) a single load cycle, immediately before the 37th propagation. 25

Figure 5.4. Size of the plastic zone at the crack tip evaluated for $a_0 = 11.5$ mm and $a_0 = 21.5$ mm considering both models: with and without GTN. 26

Figure 5.5. Comparison of CTOD predicted with and without GTN for: (a) a_0=11.5 mm, at the same load cycle of Figure 4b, (b) a_0=21.5 mm, at the same load cycles of Figure 5b (plane strain). 27

Figure 5.6. Crack closure level with and without GTN (a) a_0=11.5 mm, between the 25th and 26th crack propagations. (b) a_0=21.5 mm, between the 36th and 37th crack propagations. The results are presented in percentage up to propagation. 28

Figure 5.7. Effect of crack closure on plastic strain evolution, for $a_0 = 11.5$ mm. (a) Period between the 25th and the 26th crack propagations; (b) A single load cycle, before the 26th crack propagation. 29

Figure 5.8. Effect of crack closure on da/dN values (model with GTN). 30

Figure 5.9. da/dN-ΔK curves in log-log scale (plane strain; $F_{min} = 4.17$ N; $F_{max} = 41.7$ N; $R = 0.1$). The Paris-Erdogan law parameters are shown on the equation related to the trend-line added to the experimental results. 31

Figure 5.10. Porosity evolution with plastic strain growth for different initial crack lengths (a_0) in natural scales. Crack closure is enabled. 32

Figure 5.11. (a) Stress triaxiality throughout the entire propagation studied in Figure 5.2. (b) Porosity evolution for the same propagation. 33

Figure 5.12 Fatigue crack growth rate in terms of the initial porosity for two distinct crack lengths (a_0=11.5 mm and a_0=19 mm). Results are shown in natural scales.

Nucleation and coalescence are disabled .... ($q_1=1.5$, $q_2=1$, $q_3=2.25$. $F_{max}=41.67$, $F_{min}=4.17$, $R=0.1$, plane strain state). 35

Figure 5.13. Porosity growth due to the accumulation of plastic strain for distinct values of $f0$ for: (a) a_0=11.5 mm and (b) a_0=19 mm. Results are shown in natural scales. 36

Figure 5.14. Plastic strain accumulation vs pseudo-time for the different values of $f0$ for both crack lengths. (a) a_0=11.5 mm (b) a_0=19 mm 37

Figure 5.15. Crack closure level for: (a) a_0=11.5 mm (b) a_0=19 mm. 38

Figure 5.16. *da/dN* in terms of each Tvergaard parameter for a_0=11.5 mm. Results are shown in natural scales. Nucleation and coalescence are disabled. When q_1 is changed: q_2=1 and q_3=2.25. When q_2 is changed: q_1=1.5 and q_3=2.25. When q_3 is changed: q_1=1.5 and q_2=1. (f_0= 0.01). 39

Figure 5.17. (a) Plastic strain evolution for distinct values of q_1. The $q_1=2$ curve is almost indistinguishable because it is overlapped by the others. (b) Porosity evolution due to the increase in plastic strain. Results are shown in natural scales. 40

Figure 5.18. (a) Plastic strain evolution in terms of the distinct values of q_2. (b) Porosity evolution, due to the increase in plastic strain, for the same values of q_2 previously referred. Results are shown in natural scales. 41

Figure 5.19. Crack closure level for distinct values of q_2. Results are presented in terms of the percentage of load cycles completed to the load cycles needed to propagation to occur. 42

Figure 5.20. (a) Plastic strain evolution in terms of the distinct values of q_3. (b) Porosity evolution, due to the increase in plastic strain, for the same values of q_3 previously referred. Results are shown in natural scales. 42

Figure 5.21. *da/dN* in terms of fN, for an initial crack length of 11.5 mm in: (a) log-log scales; (b) natural scales. Coalescence is disabled ($q_1=1.5$, $q_2=1$, $q_3=2.25$, f_0=0.01, εN =0.25 and sN=0.1). 43

Figure 5.22. (a) Evolution of plastic strain for the same entire propagation depending on the fN value. (b) Evolution of porosity in terms of plastic strain for the different values of fN, porosity is in logarithmic scale. 45

Figure 5.23. Crack closure through the same propagation studied in Figure 5.11 45

Figure 5.24. *da/dN* in terms of different values of εN. Results are presented in natural scales. Coalescence is disabled, $q_1=1.5$, $q_2=1$, $q_3=2.25$, f_0=0.01, fN =0.01 and sN=0.1 46

Figure 5.25. (a) Evolution of plastic strain for the same entire propagation depending on the εN value. (b) Evolution of porosity in terms of plastic strain for the different values of εN. All the results are in natural scales. 47

Figure 5.26. Effect of sN on *da/dN*. Results are presented in natural scales for three distinct values of sN: 0.01, 0.1 and 0.2. Coalescence is disabled, $q_1=1.5$, $q_2=1$, $q_3=2.25$, f_0=0.01, fN =0.01 and εN=0.25 48

Figure 5.27. (a) Plastic Strain evolution throughout a single propagation for the three values of sN. (b). Porosity build-up for the same propagations referred before. Results are presented in natural scales. 49

Figure 5.28. Porosity accumulation due to the occurrence of plastic strain at the Gauss point located immediately after the node containing the crack tip........................ 50

Figure 5.29. Sensitivity analysis carried out on the following parameters: $f0 = 0.01$; $q1 = 1.5$; $q2 = 1$; $q3 = 1.5625$; $fN = 0.01$; $\varepsilon N = 0.25$ and $sN = 0.1$ 51

LIST OF TABLES

Table 4.1. Elastic-plastic properties of 2024-T351 aluminium alloy and parameters for the Swift isotropic hardening law combined with the Armstrong–Frederick kinematic hardening law. 18

Table 4.2. The parameters of the GTN model for the of 2024-T351 aluminium alloy....... 18

LIST OF SIMBOLS AND ACRONYMS/ ABBREVIATIONS

Symbols

$A_\mathrm{N}, B_\mathrm{N}$ – Nucleation Proportionality Constants

a – Initial crack length

a_0 – Initial crack length

x, n – Swift law material parameters

C, m – Constants of the Paris-Erdogan law

C_X – Parameter of the Armstrong & Frederick kinematic law

da/dN – Fatigue crack growth rate

f – Void volume fraction

f_0 – Initial void volume fraction

f_c – Critical void volume fraction

f_f – Fracture void volume fraction

f_N – Total void volume fraction that can be nucleated by the plastic strain rate

f_P – Total void volume fraction that can be nucleated by the mean stress rate

f^* – Effective porosity

$\dot{f}^g$ – Effective porosity due to growth of micro-voids

$\dot{f}^n$ – Effective porosity due to nucleation of micro-voids

F_max – Maximum load in a loading cycle

F_min – Minimum load in a loading cycle

F_open – Crack opening load

K – Stress intensity factor

K_C – Fracture toughness

K_max – Maximum stress intensity factor

K_min – Minimum stress intensity factor

K_open – K value where the crack opens

U^* – Portion of load cycle during which the crack is closed

R – Stress ratio

s_N, s_P – Standard deviations (Gaussian distribution) of the nucleation process

$\boldsymbol{X}$ – Deviatoric back-stress tensor

X_{Sat} – Kinematic saturation stress

Y – Geometric parameter

Y_0 – Isotropic saturation stress

$\Delta\delta_\mathrm{p}$ – Plastic CTOD range

ΔK – Stress intensity factor range

ΔK_eff – Effective stress intensity factor range

ΔK_th – Fatigue threshold

ΔN – Number of load cycles

p – Hydrostatic-pressure

$\dot{p}$ – Increment of the hydrostatic-pressure

q_1, q_2, q_3 – Void interaction parameters

$\dot{\boldsymbol{\varepsilon}}^p$ – Plastic strain rate tensor

ε_N – Mean nucleation strain

$\varepsilon_\mathrm{c}^\mathrm{p}$ – Equivalent critical plastic strain

$\dot{\boldsymbol{\varepsilon}}_d{}^p$– Deviatoric component of the plastic strain rate tensor

$\dot{\boldsymbol{\varepsilon}}_v{}^p$– Volumetric component of the plastic strain rate tensor

$\bar{\varepsilon}^p$ – Accumulated equivalent plastic strain

$\dot{\bar{\varepsilon}}^p$ – Equivalent plastic strain rate

J_3^Σ – Third invariant of the stress tensor

$\boldsymbol{\sigma}$ – Stress tensor

$\boldsymbol{\sigma}'$ – Deviatoric component of the Cauchy stress tensor

$\bar{\sigma}$ – von Mises Equivalent stress

σ – Nominal stress

σ_max – Maximum stress

σ_min – Minimum stress

δ_p – Plastic CTOD

σ_P – Mean nucleation stress

σ_y – Equivalent yield stress

ν – Poisson´s ratio

∇f – Sensitivity coefficient

λ – Constant

$\dot{\gamma}$ – Plastic multiplier

Acronyms/Abbreviations

3D – Three-Dimensional

AA – Aluminium Alloy

CJP – Christopher James Patterson (model)

CTOP – Crack Tip Opening Displacement

DD3IMP – Deep Drawing 3D IMPlicit finite element solver

FCG – Fatigue Crack Growth

FCGR – Fatigue Crack Growth Rate

FEM – Finite Element Method

GTN – Gurson-Tvergaard-Needleman

IPS – Incrementative Plastic Strain

LEFM- Linear Elastic Fracture Mechanics

SSY – Small Scale Yielding

TPS – Total Plastic Strain

RVE- Representative Volume Element

1. INTRODUCTION

Fatigue is, terminologically, the failure of a component or structure under a cyclic, either constant or varying, load which never reaches a sufficient level to cause failure on a static application. Being such a prevalent failure mechanism, design against fatigue is fundamental in most mechanical engineering projects, particularly in the case of the automotive, aeronautical and nuclear industries.

The damage tolerance approach is widespread in industry. It allows the existence of small cracks, whose presence must be evaluated through periodic inspection. This strategy is of particularly interest in areas where the occurrence of defects, which may evolve into cracks, is inevitable, such is the case of welding, casting [1] and addictive manufacturing [2]. Once the defects are detected, its evolution must be predicted. This process is influenced by several conditions, namely: the geometry of the structure or component, the configuration of the initial crack, loading history and mechanical behaviour of the materials [3].

The fatigue crack growth (FCG) process is widely evaluated using the stress intensity factor range (ΔK). This concept is interesting because it is related to the stress and strain fields occurring near the crack tip. Moreover, the fatigue crack growth rate (FCGR) is usually accessed through the da/dN-ΔK curves, which are correlated in several propagation laws [4]–[6]. Despite the importance of ΔK, it has some well-known limitations in the study of stress ratio effects, short cracks and load history effects associated with variable amplitude loading [7]. Other methodologies appeared in a tentative to overcome this limitations, such as the crack closure concept, T-stress, CJP model, integral J, energy dissipated at the crack tip and Crack Tip Opening Displacement (CTOD) [8].

The study of the non-linear crack tip phenomena emerged as an alternative to the study of FCGR based on ΔK. Different non-linear parameters have been used, namely the range of cyclic plastic strain [9], the size of the reverse plastic zone [10] and the total plastic dissipation per cycle [11]. The plastic Crack Tip Openening Displacement ($CTOD_P$) has also been used to predict FCG [12–15]. This way, the plastic deformation at the crack tip can be understood as the main driving force behind FCG [16]. In this line of work, models regarding the cumulative plastic strain prove to provide results in reasonable agreement with the experimental trends [17]–[19]. However, the comparison with experimental results showed that the effect of stress ratio was lower than obtained experimentally, particularly for Ti-6Al-4V alloy [20]. Besides, the slopes of experimental da/dN-ΔK curves were found to be higher than the slopes predicted numerically for the Ti-6Al-4V alloy [21] and the 2024-T351 aluminium alloy [17]. In other words, an anti-clockwise rotation of predicted *da/dN-ΔK* curve (Paris regime) is needed to improve the fitting to experimental results. These difficulties indicated that cyclic plastic deformation does not characterize completely the crack tip damage, and that other mechanisms are needed.

Under the presence of high levels of plastic strain, the processes of growth, nucleation and coalescence of micro voids are of great importance, due to its influence on the behaviour of the material. The quantification of this influence is made through an entity called damage [22]. The damage accumulation mechanism is usually modelled with the so called damage models, being GTN (Gurson-Needleman-Tvergaard) one of the most famous [23]. Damage accumulation is not only accounted for failure criteria [24] but also for the decrease in material stiffness, strength and a reduction of the remaining ductility [25]. Thus, the implementation of the GTN model is expected to influence *da/dN*, especially for higher Δ*K* levels, and to contribute to the true understanding of the FCG process.

This study aims to access the influence of the introduction of the GTN damage model on the FCG predicted by a node release numerical model. The cyclic plastic strain at the crack tip is considered the FCG driving force whereby the damage accumulation accounts for the material loss of strength. The relation between porosity, plastic strain and stress-triaxiality is another object of this study, defining another step towards understanding the mechanisms behind FCG. Finally, the influence of each GTN parameters on FCGR is accessed to understand how the processes of growth and nucleation of micro-voids influence the FCG.

2. LITERATURE REVIEW

2.1. Fatigue Phenomenon

In structural mechanics, where components are subjected to monotonic or static loadings, the mechanical design is achieved by specifying the maximum stress, or strain, sustainable by the components. However, in dynamic loadings the previously referred criteria are no longer appropriate. In the presence of cyclic loads, there is a progressive deterioration of the materials leading to failure for stresses, sometimes, well below the yielding stress. Moreover, fatigue is known to be the cause of 80% to 90% of the failures that occur in mechanical components operating at ambient temperature [26].

Fatigue is caused by the nucleation of a crack which, by means of cyclic stresses, propagates in the component. When the resistant area – part of the cross-section that is not cracked - is unable to support the applied load, fracture occurs suddenly. Fatigue phenomenon can therefore be divided in the following 4 steps:

- Crack initiation
- Microscopic growth
- Crack propagation
- Final fracture

2.2. Linear Elastic Fracture Mechanics

Fracture mechanics analyses materials containing one or more cracks to predict the conditions when failure is likely to occur [27]. Its development began in the early 50's. Later it was applied to fatigue phenomenon with the purpose of predicting crack propagation in materials and develop damage tolerant design strategies.

The first steps on the Linear Elastic Fracture Mechanics - LEFM - field were taken by Griffith [28]. Based on Continuum Mechanics principles, he stated that a crack only propagates if it results in a decrease on the total energy of the system. However, this energy balance only considers the equilibrium between two terms: the reduction on the elastic strain energy due to the presence of a crack on the component; and the surface energy released upon the formation of the crack flanks. This way, Griffith's theory is only valid on purely elastic bodies, where no plastic strain occurs at the crack tip.

Irwin [29] suggested that most of the energy dissipated, during crack propagation, is related to the plastic strain occurring near the crack tip. However, if the plastic strains near the crack tip affect the stress field only within small distances, in comparison to the crack length, the influence of these plastic strains will be also small. This way, the stress field near the crack tip could be predicted by linear elasticity theory and described through the stress intensity factor, *K*. [30]

$$K = Y\sigma\sqrt{\pi a}, \tag{2.1}$$

where Y is a geometric factor, σ is the nominal stress applied and a the crack length.

The stress intensity factor controls the stress and strains field near the crack tip. This way, for two distinct cracks sharing the same *K*, similar stresses and strains can be found at the vicinity of the crack tip [31]. Also, it is supposed to control the FCG [32].

In cyclic loading conditions, varying between the maximum and minimum stress intensity factors - $K_{\max}$ and $K_{\min}$ respectively-, the stress intensity factor range, ΔK, can be defined as:

$$\Delta K = K_{\max} - K_{\min}, \tag{2.2}$$

Applying a stress intensity factor range to a material, for a certain number of cycles, drives a certain crack to grow in length. The increase in length of the crack can be related to the applied cycles through the crack growth rate, da/dN-ΔK curves, as shown in Figure 2.1 [33]. Typically, three regions can be distinguished:

- Threshold Region: below the fatigue threshold, ΔK_{th}, no propagation occurs. Once this value is surpassed there is a strong increase in da/dN with ΔK.
- Paris-Erdogan Regime: Paris-Erdogan law defines the linear relation, in log-log scale, between da/dN and ΔK [5].

  $$\frac{da}{dN} = C(\Delta K)^m, \tag{2.3}$$

  C and m are material constants that depend on the environmental conditions and stress ratio.

- Accelerated Region: When $K_{\max}$ approaches the fracture toughness, K_{c}, there is a sudden increase in da/dN until fracture occurs. K_{c} is a material parameter that depends on the loading conditions or crack length.

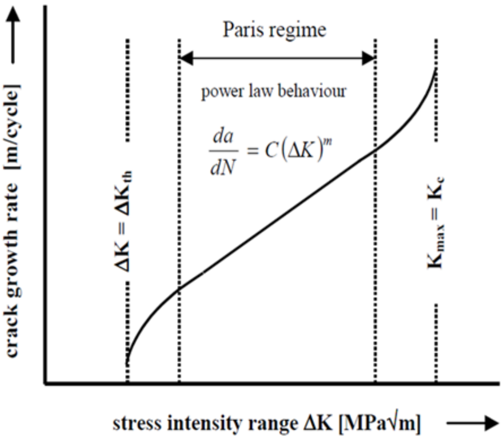

Figure 2.1 Fatigue crack growth curve. Log-log scale. Adapted from [33].

LEFM assumes the stress near the crack tip to be purely elastic. However, due to the singularity occurring at the crack tip, theoretically the stress tends to be infinitely large. This way, even if the remote stress applied to the body is small, at the vicinity of the crack tip, there should be a plastic region. This region is not taken in account by LEFM. So, the error induced, by underestimating it, is only slight when the dimensions of the plastic region are small in comparison to the remaining dimensions of the body - Small Scale Yielding (SSY) [34].

2.2.1. Crack Closure effect on LEFM

As referred, the da/dN-ΔK approach is widely used. Nevertheless, there are several problems regarding this approach, namely: the inability to predict the influence of stress ratio and load history on da/dN-ΔK relations; the odd behaviour observed for short cracks; the dimensional problems of da/dN-ΔK relations and the validity limited to LEFM. In fact, FCG is linked to nonlinear and irreversible mechanisms happening at the crack tip, while ΔK is an elastic parameter [35].

Crack closure was one of the most important concepts that emerged from the attempt to broaden the applicability of the ΔK approach. Christensen [36] proposed that the fracture surface interaction outcomes in a decrease on the stress intensity factor range at the crack tip. According to Elber [37][38] as the crack propagates, a residual plastic wake is formed. The deformed material acts as a wedge behind the crack tip and the contact of fracture surfaces is forced by the elastically deformed material. Even in tensile load a crack can be closed due to crack closure effect. Moreover, the crack only propagates on the portion of the cycle during which the crack is open, explaining how stresses lower than the crack opening stress are insufficient to propagate the crack. This fact led to the introduction of the effective stress intensity factor, ΔK_{eff}, given by:

$$\Delta K_{\text{eff}} = K_{\max} - K_{\text{open}}, \tag{2.4}$$

where K_{open} represents the stress intensity factor below which the crack remains closed. The *da/dN*-ΔK_{eff} approach proposes the replacement, in Paris Law, of ΔK by ΔK_{eff}.

$$\frac{da}{dN} = C(\Delta K_{\text{eff}})^m. \tag{2.5}$$

Crack closure is able to explain the influence of mean stress in both regimes I and II of crack propagation [39], the transient crack growth behaviour following overloads [40], the growth rate of short cracks [41], and the effect of thickness on fatigue crack growth [42]. The causes of crack closure have been attributed to PICC (plasticity induced crack closure), OICC (oxide-induced crack closure) and RICC (roughness-induced crack closure) [43]. The OICC greatly depends on the pair material-environment. According to Suresh [44] the formation of oxide films, that represents a relevant mechanism of closure, benefits from the low crack growth rates that occur near threshold. Gray [45] shown that microstructures that form rougher fracture surfaces reduce the ΔK_{eff} at the crack tip, due to crack tip impingement. Once again, RICC is more important near fatigue threshold and appears to be absent at higher stress ratios (R). Therefore, both mechanisms are more relevant in Regime I [42], where the crack opening is relatively small. On the other hand, PICC seems to be present in both Regime I and II, being the most important mechanism in Regime II [39]. The residual plastic deformation, which leads to compressive stresses behind the crack tip, raises the crack opening load on subsequent crack growths.

2.3. Elasto-Plastic Fracture Mechanics

In many materials it is theoretically impossible to characterize the FCG process based on LEFM. This is true whenever the ductility of the material induces plastic regions, at the vicinity of the crack tip, large enough to breach the SSY condition. Moreover, at this condition - Large Scale Yielding (LSY) - four different zones can be identified ahead of a fatigue crack tip, as illustrated in Figure 2.2 [46].

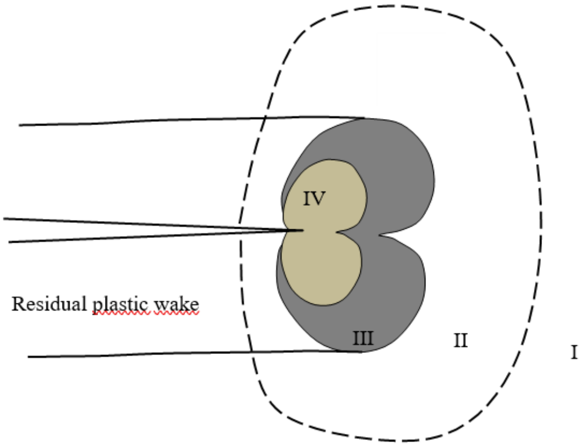

Figure 2.2. Schematic diagram of crack tip zones.

Regions I and II represent the elastic zone, which is far ahead of crack tip; the material is deformed in purely elastic regime. Region II is distinguished from the former because, here, the magnitude of the stress and strain fields is controlled by ΔK. Region III represents the monotonic plastic zone. Monotonic plastic deformation occurs during loading and after that, elastic loading-unloading takes place. Region IV, close to fatigue crack-tip, embodies the reverse/cyclic plastic zone [47]. Reverse plastic deformation occurs during unloading where the material, very near to the crack tip, suffers compressive stresses [48].

The clearly non-linear behaviour at the crack-tip prompted the search for alternative fracture-mechanics models which introduced new non-linear parameters.

2.3.1. Crack Tip Opening Displacement

Crack Tip Opening Displacement, CTOD, was firstly proposed by Wells [49] as an assess of the fracture toughness of the material through its capacity to deform plastically prior to fracture. This parameter is a measure of the displacement of the crack flanks due to the blunting suffered by an initially sharp crack.

Crack tip plastic blunting may explain the striation formation process which is verified at the fatigue crack propagation in Paris-Erdogan regime, as proposed by Laird [50]. As both phenomena are related, the CTOD concept allows the prediction of fatigue striations spacing and, therefore, the crack growth rate [51]. Moreover, Nicholls [52] proposed a polynomial relation between CTOD and crack growth rate:

$$\frac{da}{dN} = b\ (CTOD)^{\frac{1}{d}}, \tag{2.6}$$

where b and d assume the same roles of the Paris-Erdogan coefficients.

An alternative approach considers the plastic deformation at the crack tip to be the driving force behind fatigue crack growth. The plastic CTOD, δ_p, as shown by Antunes [53], is a measure of the level of plastic deformation at the crack tip. Encouraging results were attained when replacing ΔK by the plastic CTOD range, $\Delta\delta_\mathrm{p}$, in *da/dN* curves.

A *da/dN*-$\Delta\delta_\mathrm{p}$ model was developed for several materials [14], [35],[54]. In that study, the fatigue crack growth rate was obtained experimentally in C(T) and M(T) specimens. Then, the experimental tests were replicated numerically to predict $\Delta\delta_p$, which was computed at the first node behind the crack tip. The numerical models replicated the geometry of the specimen and crack, the applied load range, and the material behaviour. The *da/dN*- $\Delta\delta_\mathrm{p}$ model was used to predict the effect of stress state, stress ratio and variable amplitude loading. The trends obtained were all according to literature results [54]. Note that this is a multi-point approach because several experimental values of *da/dN* are considered to calibrate the model.

The adopted crack propagation scheme is based on a node released method. Crack growth was simulated by a successive debonding at minimum load of both current crack front nodes. Each crack increment corresponded to one finite element and two or five load cycles were applied between increments. Node release methods were firstly proposed by Newman [55] and are a very popular technique in Finite Element Method (FEM) to model crack propagation. However, as a constant FCG is assumed it does not consider the physics behind the process since the crack extension per cycle should depend on crack tip strain [18]. In fact, the crack propagation is only done to stabilize crack tip plastic deformation and crack closure level.

2.3.2. Crack Tip Plastic Strain

Pokluda [56] stated that the crack driving force in fatigue is directly related to the range of cyclic plastic strain. Thus, a model similar to the one presented in the previous section was developed based on the cumulative plastic strain [17]. However, instead of considering an arbitrary number of cycles between each propagation, the crack tip node is released when the accumulated plastic strain reaches a critical value. Nevertheless, the comparison and consequent release is only performed when the load is at minimum to avoid eventual convergence problems related to crack propagation at maximum loads [57]. Due to the singularity at the crack tip, the equivalent plastic strain is defined as the average measured at the Gauss points immediately behind and ahead of the crack tip node. The critical plastic strain is supposed to be a material property, which is calibrated using only a single experimental value of da/dN.

The discussed method may follow two distinctive approaches. Incremental Plastic Strain (IPS) considers the accumulated plastic strain to be set to zero after each crack node release. This means that the plastic deformation that occurred previously at the Gauss point surrounding the crack tip only affects the material hardening. IPS approach assumes the FCG to be due to the irreversible strain acting at the crack tip. Alternatively, Total Plastic Strain (TPS) approach considers the cumulative sum of all the plastic strain developed at the Gauss points, even when they do not contain the crack tip. Thus, the propagation is assumed to be due to the damage accumulation induced by cyclic plastic strain [21].

2.4. Other mechanisms affecting FCG

Cyclic plastic deformation is generally accepted as the most important crack tip mechanism responsible for FCG [16]. However, environmental damage is supposed to have a significant contribution particularly near ΔK_{th} [58]. At high load levels, brittle failure and growth and coalescence of micro voids are possible mechanisms since they greatly depend on maximum load.

Borges [17] suggested that the difference between experimental and numerical results, obtained with the models based on cumulative plastic strain, must be linked to mechanisms controlled by $K_{\max}$. Additionally, Pippan [59] found a strong relation between $K_{\max}$ and the fatigue propagation rate of brittle materials. According to Newman [60], the fatigue crack growth rate, of an Aluminium alloy, near the fatigue threshold was exacerbated by increased levels of $K_{\max}$. Despite the proven influence of $K_{\max}$ in FCG, the numerical results indicate that $K_{\max}$ has no effect on cyclic plastic deformation at the crack tip [61]. Therefore, alternative damage mechanisms are required to explain it. Possible mechanisms, driven by $K_{\max}$, are the growth and coalescence of microvoids, diffusion-based mechanisms and brittle failure. Accordingly, this work will be focused on evaluate the effect of the growth and coalescence of micro voids on the FCG, a mechanism associated with ductile fracture.

2.5. Physical mechanisms of the ductile fracture

Ductile fracture is a mechanism that involves three stages: nucleation, growth and coalescence of cavities [62]. Voids are defects innate to the materials. However, the amount of voids tend to increase when high levels of plastic deformation occur. In this case, void initiation arise by fracture of non-metallic inclusions and by the decohesion of the inclusion-matrix interface [63], [64]. Under certain conditions voids will subsequently grow.

McClintock states that stress and strain histories importantly affect the size, shape and distribution of voids in the materials [65]. Moreover, the stress state is of major importance in ductile fracture [66]. The deviatoric component is primarily responsible for void nucleation; while the hydrostatic stress dictates the void growth and coalescence steps [67]. Hence, the stress triaxiality dictates which are the active mechanisms behind void growth. Under low stress triaxiality, voids suffer changes in shape without affecting the void volume fraction. Therefore, fracture is mainly due to shape changing void growth [68]. Alternatively, on the presence of high stress triaxiality, as it occurs at a fatigue crack tip [69], voids dilatate without changing their shape [70]. Increasing the loading, voids become so large that start interacting with each other, occurring coalescence.

In the coalescence stage the growing voids link together leading to the formation (or propagation) of macroscopic cracks and, ultimately, the fracture of the material [66]. Once again, the active phenomena behind void coalescence are affected by the stress triaxiality. In *Void impingement* mechanism, voids simply touch and coalesce in a larger cavity. *Internal necking* occurs for highly triaxial stress states and consists in the neck down of the matrix ligaments between two voids [71]. Finally, *void sheet* is the main mechanism at low stress triaxialities. Second generation voids are nucleated at high concentration shear bands due to strain localization between larger cavities. Impingement occurs locally by fracturing the 2D surface defined by the strain localization region where newer voids have been nucleated [66]. This mechanism is not exclusive to shear loading.

The progressive deterioration of the material due to the mechanisms of nucleation, growth, and coalescence of voids is generally named *damage* [72]. The alternative FCG mechanisms, referred in the previous section are highly connected to the accumulation of damage. Thus, to assess the importance of these mechanisms, it is crucial to consider a *Damage Model* in the numerical analysis of FCG.

2.6. A Brief Background on Damage Models

Damage models describe the failure process by means of damage evolution [73]. Damage is macroscopically related to a decrease in the material stiffness, strength and remaining ductility [25]. However, despite the importance of these effects, which are physically measurable, this variable is not easily assessable. Damage is proposed to be linked to continuous solid mechanics variables as stress and strain [74] and can be evaluated using either coupled or uncoupled models.

Uncoupled models predict the fracture initiation, upon the onset of micro void coalescence, by means of a fracture criterion in the post processing step [75]. Damage is considered independent of the material plastic behaviour, i.e. the damage accumulation do not affect the material plastic properties [72]. According to these models, fracture occurs when the cumulative damage exceeds a critical value [76]. On the other hand, the coupled models are interconnected with the material constitutive equations through the damage accumulation due to micro void nucleation, growth and coalescence. Thus, the mechanical response of the materials is a function of damage. These models can be classified into damage-based models and micromechanical-based[75].

Damage-based models derive from classical continuous damage mechanics. This approach, as proposed by Lemaitre [77], macroscopically defines a damage variable as an effective surface density of cracks within a plane. Other similar methods aggregate the phenomena behind nucleation, growth and coalescence mechanisms in a phenomenological law. Therefore, the constitutive models are based on the macroscopic behaviour of the material [76]. Regarding the micro-mechanical approaches, they explicitly models the material microstructure through unit cell simulations [75]. In other words, ductile failure and damage accumulation are predicted through the consideration of individual micro-defects in the material [78]. As stated before, voids are innate defects to the materials. Also, the presence of second phase particles and impurities eases the nucleation of new vacancies. In the occurrence of important plastic deformations, voids grow and eventually coalesce leading to the formation and/or propagation of micro-cracks. Thus, ductile fracture, material porosity and micro-voids are intimately related [79]. This is the main advantage of micro-mechanical damage models: being able to describe the evolution of damage on a material, through the void's distribution, allows the accurate prediction of ductile failure. Since it is not computationally feasible to take in account each void in the material, the influence of the voids is incorporated into the constitutive models [80].

In this study, the coupled micromechanical damage model initial developed by Gurson and further improved by Tvergaard and Needleman is adopted in the numerical analysis of FCG [81].

3. GTN DAMAGE MODEL

Using micro-mechanical considerations, Gurson [82] developed a model which introduced a new yield surface for materials containing either spherical or cylindrical voids. The yield criterion was derived by performing an upper bound limit load analysis on the representative volume elements (RVE) - either a spherical void within a spherical RVE or a cylindrical void within a cylindrical RVE. The matrix was assumed to be free of voids and obeyed the pressure insensitive von Mises criterion. Finally, the pressure sensitive yield surface, which takes in account the damage accumulation, was achieved assuming a flow rule [70][72].

The Gurson yield surface is given, for spherical voids, by [83]:

$$\phi = \left(\frac{\bar{\sigma}^2}{\sigma_{\mathrm{y}}}\right)^2 + 2f \cosh\left(\frac{\operatorname{tr} \boldsymbol{\sigma}}{2\sigma_{\mathrm{y}}}\right) - 1 - f^2 \ , \tag{3.1}$$

where f is the void volume fraction, $\bar{\sigma}$ is the von Mises equivalent stress, $\operatorname{tr} \boldsymbol{\sigma}$ the trace of the stress tensor and σ_{y} the flow stress given by the hardening law. The assumed flow rule is expressed by:

$$\dot{\boldsymbol{\varepsilon}}^p = \dot{\gamma}\frac{\partial \phi}{\partial \boldsymbol{\sigma}} = \dot{\boldsymbol{\varepsilon}_d}^p + \dot{\boldsymbol{\varepsilon}}_v{}^p = \dot{\gamma}\boldsymbol{\sigma}' + \frac{1}{3}\dot{\gamma} f \sigma_{\mathrm{y}} \sinh\left(\frac{3p}{2\sigma_{\mathrm{y}}}\right)\boldsymbol{I} \ , \tag{3.2}$$

where the plastic strain rate tensor, $\dot{\boldsymbol{\varepsilon}}^p$, involves two terms: the deviatoric, $\dot{\boldsymbol{\varepsilon}_d}^p$, and volumetric, $\dot{\boldsymbol{\varepsilon}}_v{}^p$, plastic strains. $\dot{\gamma}$ is the plastic multiplier, p the hydrostatic-pressure, $\boldsymbol{\sigma}'$ the deviatoric stress tensor and $\boldsymbol{I}$ the identity matrix [84].

The evolution law for the void volume fraction is given, for the original Gurson's model, by:

$$\dot{f} = (1-f)\dot{\boldsymbol{\varepsilon}}_v{}^p = (f - f^2)\dot{\gamma}\sigma_{\mathrm{y}} \sinh\left(\frac{3p}{2\sigma_{\mathrm{y}}}\right), \tag{3.3}$$

Adjustments to the initial yield surface were proposed by Tvergaard [85] [86] to better represent the material response predicted by numerical cell studies [87].

$$\phi = \left(\frac{\bar{\sigma}^2}{\sigma_{\mathrm{y}}}\right)^2 + 2q_1 f \cosh\left(q_2\frac{\operatorname{tr} \boldsymbol{\sigma}}{2\sigma_{\mathrm{y}}}\right) - 1 - q_3 f^2 \ , \tag{3.4}$$

q_1, q_2 and q_3 are designated void interaction parameters, as they adjust Gurson's yield surface to account for the influence of neighboring voids.

In Gurson’s criterion, the mechanisms of ductile fracture are modelled by explicitly monitoring the void volume fraction [72]. However, no void volume fraction evolution will be predicted if the initial void ratio is zero. Thus, several mechanisms were proposed to modify the model in order to consider void nucleation, depending on strain history [84]. Chu and Needleman [88] proposed the most widely used nucleation law, which considers nucleation, following a normal distribution, in a statistical way. Later, Tvergaard and Needleman [89], using this nucleation law, modified Gurson’s criterion to account for the onset of void coalescence prior to material fracture.

$$\phi = \left(\frac{q^2}{\sigma_{\mathrm{y}}}\right)^2 + 2q_1 f^* \cosh\left(q_2 \frac{\operatorname{tr} \boldsymbol{\sigma}}{2\sigma_{\mathrm{y}}}\right) - 1 - q_3 f^{*2} \ , \tag{3.5}$$

Equation 3.6 defines the so-called Gurson-Tvergaard-Needleman (GTN) model, which considers the effective porosity, f^*:

$$f^* = \begin{cases} f & , \ f \leq f_{\mathrm{c}} \\ f_{\mathrm{c}} + \left(\frac{1}{q_1} - f_{\mathrm{c}}\right) \frac{f - f_{\mathrm{c}}}{f_{\mathrm{f}} - f_{\mathrm{c}}} & , \ f \geq f_{\mathrm{c}} \end{cases} \ , \tag{3.6}$$

where f_{c} and f_{f} represents the critical and fracture void volume fraction, respectively. The void coalescence mechanisms become active if the void volume fraction is higher than the critical value. Whenever the void volume fraction is less than the critical value, the effective porosity is attained from both void nucleation and growth mechanisms:

$$\dot{f} = \dot{f}^n + \dot{f}^g, \tag{3.7}$$

where the void growth mechanism is given by Equation 3.4. On the other hand, the nucleation mechanism was defined by Chu and Needleman, which is driven either by plastic strain or hydrostatic pressure:

$$\dot{f}^n = A_{\mathrm{N}} \dot{\bar{\varepsilon}}^p + B_{\mathrm{N}} \dot{p}, \tag{3.8}$$

where $\dot{\bar{\varepsilon}}^p$ represents the rate of the accumulated plastic strain and $\dot{p}$ the increment of the hydrostatic pressure. The proportionally constants A_{N} and B_{N} are given by:

$$A_{\mathrm{N}} = \begin{cases} 0 & , \ p < 0 \\ \frac{f_{\mathrm{N}}}{s_{\mathrm{N}}\sqrt{2\pi}} \exp\left[-\frac{1}{2}\left(\frac{\dot{\bar{\varepsilon}}^p - \varepsilon_{\mathrm{N}}}{s_{\mathrm{N}}}\right)\right] & , \ p \geq 0 \end{cases} \ , \tag{3.9}$$

$$B_{\mathrm{N}} = \begin{cases} 0 & , \ \dot{p} < 0 \\ \frac{f_{\mathrm{P}}}{s_{\mathrm{P}}\sqrt{2\pi}} \exp\left[-\frac{1}{2}\left(\frac{p - \sigma_{\mathrm{P}}}{s_{\mathrm{P}}}\right)\right] & , \ \dot{p} \geq 0 \end{cases} \ , \tag{3.10}$$

ε_{N} and σ_{P} are the mean value of the Gaussian distribution. s_{N} and s_{P} represent the standard deviations. f_{N} and f_{P} are the total void volume fraction that can be nucleated by the plastic strain rate and by the mean stress rate, respectively [72].

3.1. Calibration of the GTN model parameters

The GTN model has a total of twelve parameters:

- the void interaction parameters which characterise the yield behaviour of the materials (q_1, q_2 and q_3)
- the material parameters, used to model void nucleation ($\varepsilon_N, \sigma_{\mathrm{P}}, s_{\mathrm{N}}, s_{\mathrm{P}}, f_{\mathrm{N}}$ and f_{P})
- ductile fracture parameters that describe the evolution of void growth up to coalescence and final failure (f_{c} and f_{f})
- the initial porosity of the material (f_0)

Often, the identification of all the twelve parameters of the GTN model is an overly complex approach [90]. Thus, for the void interaction parameters it is common to consider the values recommended by Tvergaard [86]: $q_1 = 1.5$; $q_2 = 1.0$; $q_3 = 2.25$ [91][92]. The material parameters can be identified by measuring changes on displacement fields, forces and moments [93] or by metallurgical observations [92][23]. In these approaches the parameters are found by fitting numerical and experimental curves through optimization algorithms. To reduce the number of material parameters it is usual to consider $\varepsilon_{\mathrm{N}} = 0.3$ and $s_{\mathrm{N}} = 0.1$ [94]. The ductile fracture parameters may be determined from numerical simulations at the point where the model attains the displacement to fracture, experimentally observed [95][96].

In addition to the specific parameters involved in GTN model, the hardening law of the matrix material has also to be defined. In case of monotonic loadings, the hardening law parameters may be calibrated to fit the stress-strain curve of the actual porous material obtained from quasi-static uniaxial tensile tests of un-notched specimens up to necking [72]. More recently, genetic and machine learning algorithms allowed the identification of the coupled GTN model parameters in a timely manner [97][98].Nevertheless, these methods require much data, regarding the material mechanical response, which has to be obtained through several experimental tests.

3.2. Applications and modifications to the classical GTN model

The GTN model has been used in several engineering applications, namely: the failure prediction in welded joints [87], rolling [99], forging [100] and sheet metal forming processes [101][102], fatigue life predictions [103], etc. Despite its widespread use, the GTN model has some drawbacks and has undergone several changes through time.

The GTN model identifies the effective porosity as fracture driving force. An increase in f^*, due to void growth, requires a positive mean stress. Thus, in low triaxial and shearing loadings, under zero mean pressure, the model predicts no increase in damage [104]. Accordingly, some modifications to the classical GTN model have been suggested. Nahshon [105] proposed an extension of the Gurson model that incorporates damage growth under low triaxiality straining for shear-dominated states. Xue [106] introduced a separate internal damage variable which differs from the conventional void volume fraction.

In Gurson-type models, yielding, void evolution and strain to fracture depend only on the stress triaxiality [105]. However, Cazacu [107] shown that, for the same stress triaxiality, there are two axisymmetric stress states that can only be distinguishable by the sign of the third invariant of the stress tensor, J_3^{Σ}. This way, stress triaxiality by itself is insufficient to characterize yielding. Moreover, Alves and Cazacu [79] studied the effects of the coupling between the sign of the mean stress and the sign of J_3^{Σ}. The results shown that the porosity rate of growth or collapse is much faster than the achieved through the classical Gurson criterion.

4. NUMERICAL MODEL

This study considers a 2024-T351 aluminium alloy. This aluminium alloy is currently used in several engineering applications, namely in the aeronautical industry due to the high strength to weight ratio. All numerical simulations were performed with the in-house finite element code DD3IMP, originally developed to simulate deep-drawing processes [108][109]. This finite element code uses an updated Lagrangian scheme to describe the evolution of the deformation process. The mechanical model assumes the elastic strains to be negligibly small with respect to unity and considers large elastoplastic strains and rotations.

4.1. Material Constitutive Model

The mechanical behaviour of this alloy is described by a phenomenological elastic–plastic constitutive model. The isotropic elastic behaviour is given by the generalized Hooke's law. Regarding the plastic behaviour, the shape of the yield surface is defined by the von Mises yield criterion with an associated flow rule. The evolution of the yield surface during plastic deformation is described by the Swift isotropic hardening law combined with the kinematic hardening law proposed by Armstrong–Frederick. The Swift law is given by:

$$\sigma_y(\bar{\varepsilon}^p) = x\left(\left(\frac{Y_0}{x}\right)^{\frac{1}{n}} + \bar{\varepsilon}^{\mathrm{p}}\right)^n \tag{4.1}$$

where Y_0, x, and n are the material parameters and $\bar{\varepsilon}^{\mathrm{p}}$ is the equivalent plastic strain. The Armstrong–Frederick law is:

$$\dot{\boldsymbol{X}} = C_{\mathrm{X}}\left[\frac{X_{\mathrm{sat}}}{\bar{\sigma}}(\boldsymbol{\sigma}' - \boldsymbol{X})\right]\dot{\bar{\varepsilon}}^{\mathrm{p}}, \text{ with } \dot{\boldsymbol{X}}(0) = 0 \tag{4.2}$$

where $\boldsymbol{X}$ is the back stress tensor, X_{Sat} and C_{X} are material parameters, and $\dot{\bar{\varepsilon}}^{\mathrm{p}}$ is the accumulated equivalent plastic strain rate. The isotropic and kinematic hardening parameters were simultaneously calibrated using the stress–strain curves obtained in smooth specimens of the experimental low cycle fatigue tests [110]. Table 4.1 presents the list of parameters that define the hardening behaviour of this aluminium alloy.

Table 4.1. Elastic-plastic properties of 2024-T351 aluminium alloy and parameters for the Swift isotropic hardening law combined with the Armstrong–Frederick kinematic hardening law.

Material	E **[GPa]**	ν	Y_0 **[MPa]**	x **[MPa]**	n	X_{Sat} **[MPa]**	C_X
AA 2024-T351	72.26	0.29	288.96	389.00	0.056	111.84	138.80

The GTN parameters related with the growth of voids were chosen with base on the existent literature regarding this aluminium alloy [97], which are presented in Table 4.2. The initial porosity (f_0) was overestimated to the largest value range to overcome the inexistence of nucleation and coalescence.

Table 4.2. The parameters of the GTN model for the of 2024-T351 aluminium alloy.

Material	ε_N	σ_P	s_N	s_P	f_N	f_P	q_1	q_2	q_3	f_c	f_f	f_0
AA 2024-T351	0.25	800	0.1	250	0	0	1.5	1	2.25	-	-	0.01

4.2. Boundary Conditions and Geometry

Compact tension specimens, in accordance with ASTM E647 standard [111], were adopted in this study, whose geometry and main dimensions are shown in Figure 4.1. Due to the existent symmetry on the crack plane, only the upper part of the specimen was considered. To reduce the computational cost only one layer of elements was considered in the thickness direction, resulting in a specimen thickness of 0.1 mm. However, as plane strain conditions were imposed, in all simulations of the study, by constraining out of plane displacements on a both faces of the component, the obtained results are independent of the specimen thickness.

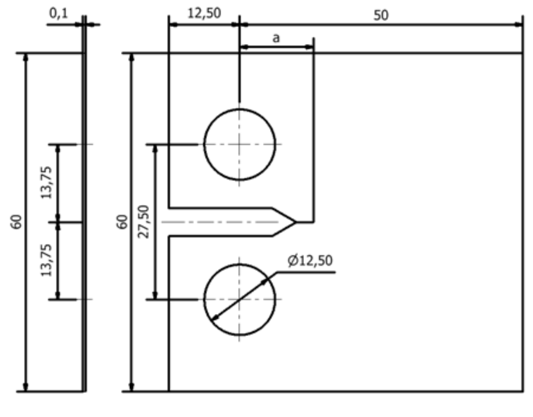

Figure 4.1. Geometry and main dimensions (in mm) of the Compact Tension specimen used in the study of the AA2024-T351. [17].

4.3. Specimen Discretization

The deformable body geometry was discretized with 8-node hexahedral finite elements, a selective reduced integration technique was adopted to avoid volumetric locking [112]. The mesh of the specimen considers three distinct zones: a very refined area near the crack tip, a transition zone, and a coarser mesh in the far side of the crack zone, as shown in Figure 4.2.

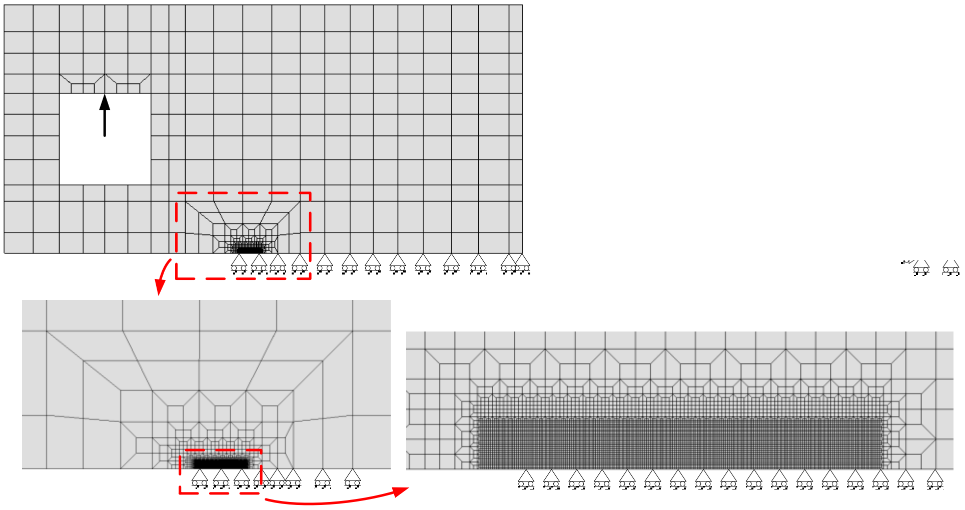

Figure 4.2. Finite element mesh of the CT specimen. The refined mesh is shown in the image on the bottom left corner. Adapted from [20].

The region surrounding the crack growth path is meshed with elements of 8 μm, which allow to accurately evaluate the strong gradients of stresses and strains in this zone [113]. Due to the singularity at the crack tip, the more one refines the mesh, in this zone, the higher will be the stress. On the other hand, the coarser zone allows to reduce the computational cost. In the end 7287 finite elements and 14918 nodes were used.

4.4. Loading Case

The specimen is loaded, considering a single point force applied on the specimen hole, with a constant amplitude cyclic load. Mode I loading is considered, and the variation range was set between $F_{\min}$=4.17 N and $F_{\max}$=41.7 N, resulting in a stress ratio, R=0.1. Some load cycles are presented, in terms of the pseudo-time in Figure 4.3.

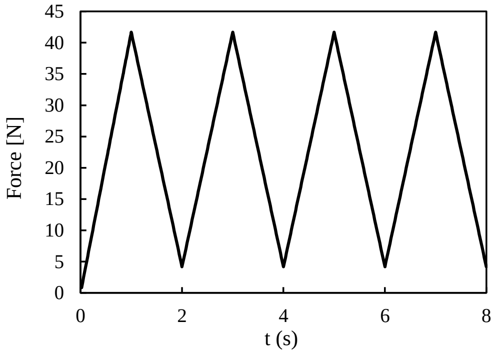

Figure 4.3. Loading cycles applied to the CT specimen. F_{min}= 4.17 N, F_{max}= 41.67 N, R=0.1.

4.5. Crack Propagation Scheme

Considering the geometry of the CT specimen and the applied loading, the crack path arises in the symmetry plane, extending over the entire specimen thickness. To simulate the continuous advance of the crack tip, the nodes over the crack path are released according to the proposed algorithm. However, the discretization of the crack path with finite elements leads to a discontinuous crack growth, i.e., each crack increment corresponds to one finite element (8 μm size).

The predicted FCG rate is obtained from the ratio between the crack increment (8 μm) and the number of load cycles, ΔN, required to reach the critical value of plastic strain:

$$\frac{da}{dN} = \frac{8\ \mu\text{m}}{\Delta N} \tag{4.3}$$

Hence, the FCG rate is assumed constant between crack increments. Since the crack propagation rate is usually relatively low (<1 μm/cycle), the numerical analysis of the crack growth is simplified by considering different sizes for the initial straight crack. The continuous advance of the crack tip is appropriately replaced by a set of small crack propagations (<500 μm), distributed over the crack path. Initial crack sizes, a_0, of 5, 9, 11.5, 16.5, 19 and 21.5 mm were considered. Since some crack propagation is required to stabilize the cyclic plastic deformation and the crack closure level, the FCG rate is evaluated only after that. Finally, the contact between the flanks of the crack is modelled considering a rigid plane surface aligned with the crack symmetry plane.

4.6. Crack Growth Criteria

In this study, crack propagation occurs when the critical plastic deformation at the crack tip is achieved, whereby the GTN damage model accounted for the progressive deterioration of the material due to plastic deformation. This criteria considers the plastic deformation to be the main driving force of the FCG, as proposed by Borges *et al* [17]. Therefore, the crack tip node is released when the accumulated plastic strain reaches a critical value. The critical plastic strain, $\varepsilon_{\mathrm{c}}^{\mathrm{p}}$, based on a previous study [17], was considered: $\varepsilon_{\mathrm{c}}^{\mathrm{p}} = 1.1$. Note that this value corresponds to a plastic strain of 110 %. Using the TPS strategy, the plastic strain accumulated in the previous load cycles, at a certain node are not reset when a propagation occurs. This strategy is adopted because the plastic strain is irreversible, allowing a more realistic modelling of the processes occurring at the crack tip.

5. NUMERICAL RESULTS AND DISCUSSION

This section starts with the comparison between the proposed numerical model with and without GTN, whereby only the process of growth of micro-voids is active. Then, the influence of stress triaxiality on the porosity evolution due to the plastic strain accumulation is evaluated, neglecting the process of coalescence in the analysis. Finally, the influence of each GTN parameter on the predicted *da/dN* is assessed, allowing to perform a sensitivity analysis.

5.1. FCG modelling with and without GTN.

5.1.1. Fatigue Crack Growth Rate

Figure 5.1 shows the *da/dN*-Δ*K* curves predicted numerically with and without GTN model. The horizontal and vertical axes are presented in log-log scales, as is usual. The *da/dN*-Δ*K* curve without GTN follows an approximately linear trend in log-log scale, through all Δ*K* values studied, with a Paris law coefficient, *m*=2.62. The inclusion of GTN damage model significant changes the predicted da*/dN*. For low values of *ΔK* there is a decrease of *da/dN* with the inclusion of the growth of micro-voids in the model, while for high values of Δ*K* the opposite trend is observed. The inversion of behaviour occurs at about Δ*K*=11.5 MPa.m$^{0.5}$. The model with GTN roughly follows a linear trend for lower values of Δ*K*, but the linearity disappears when the full range of Δ*K* is included. The Paris law coefficient is also higher (*m*=3.36).

The nucleation, growth and coalescence of micro-voids phenomena are supposed to deteriorate the material stiffness. Moreover, this ductile damage model is directly related to the plastic deformation, which is important at the crack tip. Thus, it was expected that the introduction of the GTN damage model would result in an increase in the FCGR. Nevertheless, the growth of micro-voids in the model may have a protective behaviour, reducing the FCGR. An explanation for the odd behaviour observed at relatively low values of Δ*K* is required.

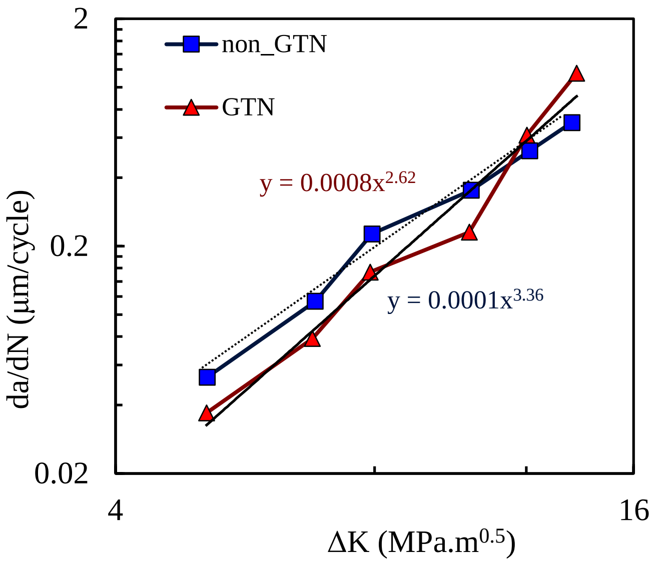

Figure 5.1. *da/dN-ΔK* curves in log-log scale (plane strain; R = 0.1; f_0 = 0.01; q_1 = 1.5; q_2 = 1 and q_3 = 2.25, nucleation and coalescence are disabled). The Paris-Erdogan law parameters are shown on the equations related to the trend-lines.

5.1.2. Cumulative Plastic Strain

To explain the influence of the GTN model on FCGR, both plastic strain and crack closure were studied for two different values of stress intensity factor. Accordingly, two initial crack lengths are evaluated, namely a_0=11.5 mm, which corresponds to a stage where the model with GTN predicts a lower *da/dN* than the model without GTN; and a_0=21.5 mm, which corresponds to the final phase of the crack growth, where the FCGR is higher with GTN (see Fig 5.1). Figure 5.2a shows the evolution of the plastic strain during the period between the 25th and 26th crack propagations. This corresponds to a steady state of the propagation, for both models (with and without GTN). Time was reset, on the instant where the previous propagation occurred, so that propagations from both models could be compared. The results show that the plastic strain presents a sudden drop at each propagation. Since this entity is evaluated at the node containing the crack tip, when propagation occurs, the crack-tip advances to the following node where the plastic strain is still small. Then, the subsequent load cycles cause the plastic strain to increase in a cumulative way. However, the plastic strain clearly grows faster in the model without GTN, i.e. the critical plastic strain is achieved faster. Once the critical strain, ε_c^p, is achieved, node release occurs for both models, and a new accumulation begins.

Figure 5.2b presents the plastic strain evolution at the crack tip during a single load cycle, immediately before the 26th crack propagation, comparing the two models. The initial constant value is due to crack closure and consequent absent of plastic deformation at the crack tip. The plastic deformation starts later in the model with GTN, which may be explained by different crack closure levels. The increase of load up to the maximum value produces an accumulated plastic strain, which is higher in the model without GTN. The same trend is followed in the unloading phase. This explains the higher slope of the plastic strain curve observed in Figure 5.2 for the model without GTN.

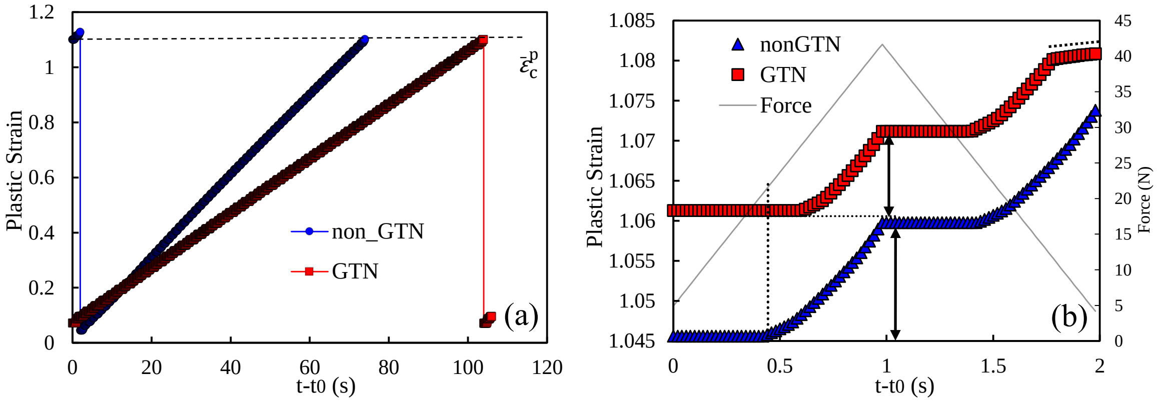

Figure 5.2. Comparison of the plastic strain evolution with and without GTN for a_0=11.5 mm. **(a)** time period between the 25th and the 26th node releases; **(b)** a single load cycle, immediately before the 26th propagation.

Figures 5.3 presents analogous results, but for a_0=21.5 mm, corresponding to the period between the 36th and the 37th crack propagations. Different propagations were chosen because the crack growth stabilization is slower for higher initial crack lengths. The values of plastic strain after each node release are higher than the ones observed in Figure 5.2a. Since the size of cyclic plastic zone increases with ΔK, larger initial plastic strains may be expected for higher ΔK levels. Moreover, the inclusion of GTN also results in a higher cumulative plastic strain in the crack tip at the beginning of the propagations, which is linked to the increase of plastic strain produced by the GTN. The application of the load cycles leads to an increase of the plastic strain in the crack tip (see Figure 5.3a). However, it grows faster using the model with GTN. Regarding the evolution of the plastic strain at the crack tip during a single load cycle, the results in Figure 5.3b show that plastic strain starts to increase at approximately the same time for both models. However, the increase of the plastic strain is much faster using the GTN model. Thus, the inclusion of the damage model has a detrimental effect on the material strength, increasing the plastic strain rate during the loading. Similar to the previous case, the same trend is verified in the unloading stage.

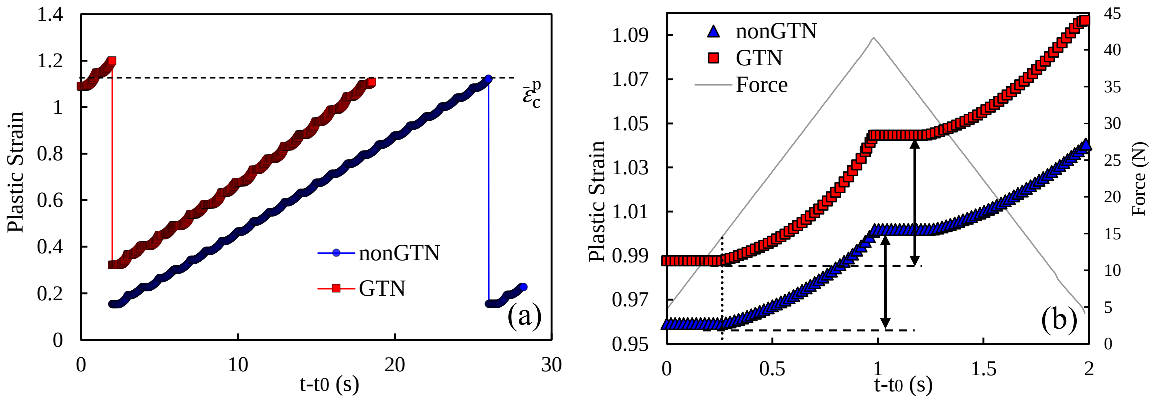

Figure 5.3. Comparison of the plastic strain evolution with and without GTN for a_0=21.5 mm. **(a)** time period between the 36th and the 37th node releases; **(b)** a single load cycle, immediately before the 37th propagation.

5.1.3. Size of the Plastic Zone at the Crack Tip

The results shown in Figure 5.2a and 5.3a indicate that the plastic strain at the beginning of each new propagation is higher in the case of the model with GTN. This is explained by the occurrence of higher plastic zones at the crack tip, which lead to sooner increments of plastic strain in farthest nodes. The distance between the node containing the crack tip and the first node exhibiting no plastic strain was measured in the propagation direction. The size of the plastic zone is presented in Figure 5.4, comparing the two crack lengths (a_0=11.5 mm and a_0=21.5 mm), as well as both models: with and without damage model. The horizontal axis presents the fraction of load cycles required to reach the critical plastic strain. Since the plastic zone size is significatively larger than the crack increment (8 μm), it is approximately constant within each propagation. On the other hand, for both initial crack lengths analysed, the model with GTN leads to larger plastic zone sizes, explaining the higher initial plastic strain at the beginning of each new propagation. Also, higher a_0 leads to higher dimensions of the plastic zone due to the higher ΔK levels occurring at the crack tip.

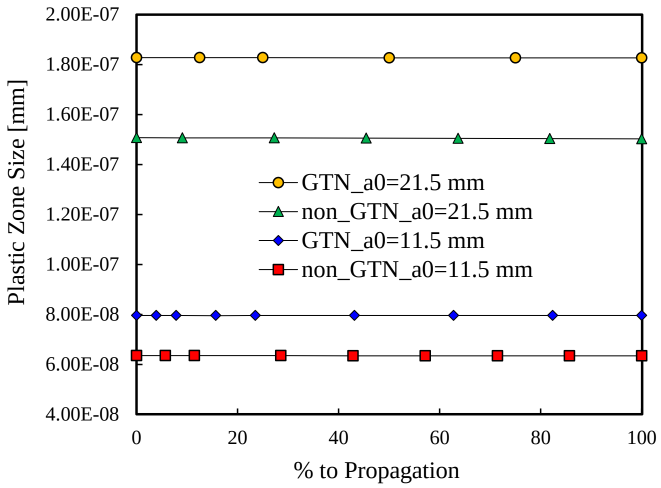

Figure 5.4. Size of the plastic zone at the crack tip evaluated for $a_0 = 11.5$ mm and $a_0 = 21.5$ mm considering both models: with and without GTN.

5.1.4. Plasticity Induced Crack Closure

The evolution of the plastic strain explains the differences in the behaviour of the da/dN-ΔK curves. Figure 5.5 presents the crack tip opening displacement (CTOD) measured at the first node behind the crack tip, at a distance of 8 µm. Figure 5.5a shows the CTOD in the last load cycle before the 26th propagation for a_0=11.5 mm, while Figure 5.5b shows analogous results but for the 37th propagation of a_0=21.5 mm. The CTOD curves were evaluated for the load cycles for which the plastic strain evolution was evaluated in Figures 5.2b and 5.3b. Considering the damage model, lower CTOD levels are predicted for both crack lengths. This can be explained by the fact that the higher plastic strain induced by the GTN results in higher plastic wakes at the crack flanks and, consequentially a higher trend to close the crack. The crack closure reduces the effective load range, protecting the material from FCG since the crack only grows when it is open. The lower growth rate of plastic strain, for a_0=11.5 mm, matches the higher closure level attained with the model considering GTN. Note that, without GTN, there is no crack closure. On the other hand, for a_0=21.5 mm the crack closure is very small, even with GTN. Thus, as the crack closure ceases to protect the material, the higher plastic strain achieved with GTN model causes a faster FCG rate.

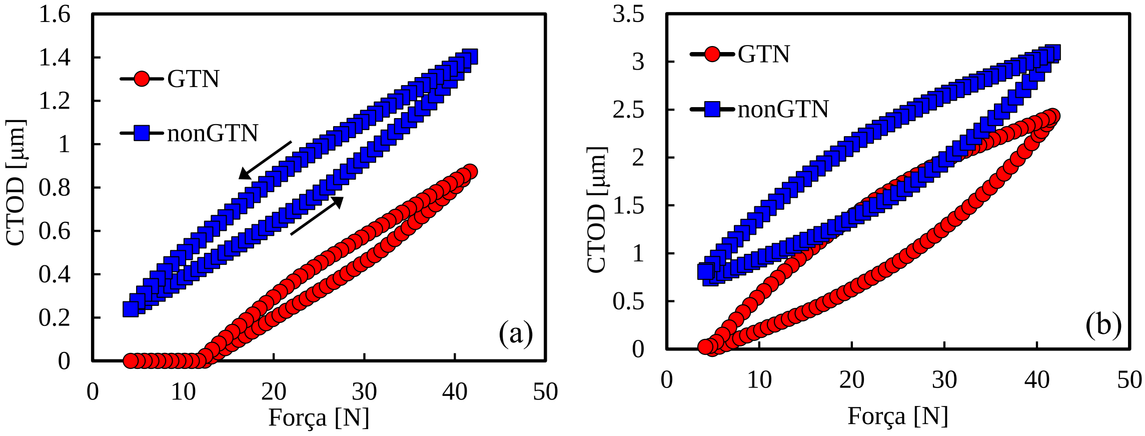

Figure 5.5. Comparison of CTOD predicted with and without GTN for: **(a)** a_0=11.5 mm, at the same load cycle of Figure 4b, **(b)** a_0=21.5 mm, at the same load cycles of Figure 5b (plane strain).

The crack closure level was evaluated during an entire propagation for both initial crack lengths, with and without GTN. The crack closure level was quantified, over the load increments, considering the contact status of the first node behind the crack tip, using the parameter:

$$U^* = \frac{F_{\text{open}} - F_{\text{min}}}{F_{\text{max}} - F_{\text{min}}} \tag{5.1}$$

where F_{open} is the crack opening load, F_{min} is the minimum load and F_{max} is the maximum load. This parameter quantifies the fraction of load cycle during which the crack is closed.

Figure 5.6a presents the crack closure evolution between the 25th and the 26th crack propagations of a_0=11.5 mm, comparing the predictions with and without damage model. Crack closure is evaluated as a function of propagation fraction, i.e., the node release occurs for 100% of propagation. A transient behaviour is registered at the beginning, consisting of a fast increase followed by a progressive decrease to a stable value. Initially, crack closure rises due to the accumulation of plastic strain and formation of residual plastic wake. During the transient stage, crack closure is very sensible to the point where it is measured. The successive load cycles cause the crack tip to blunt reducing the crack closure level. Note that the trend of the crack closure during the loading cycles is the same for both models; there is only a vertical shift of the curve referring to the model considering GTN. However, while the model without GTN completely loses crack closure, the model with GTN stabilizes at U^*=20%. Other authors also found no closure in their numerical studies without GTN, namely Zhao and Tong [114] in a CT specimen and Vor *et al.* [115] at the centre of a 3D CT specimen.

Figure 5.6b shows similar results but between the 36th and the 37th node releases of a_0=21.5 mm. For this initial crack length, the propagation with GTN takes considerably less cycles. Globally, crack closure is higher for the model with GTN. Nevertheless, the trend followed by both models is different from the one registered for a_0=11.5 mm. The initial peak is now more pronounced, which is due to the higher plastic strain produced by the harsher stress field at the crack tip induced by higher ΔK level. The subsequent decrease of U^* is a blunting effect caused by the cyclic loading, which moves the node behind crack tip [116]. This phenomenon is related with strain ratcheting, and greatly depends on material, being more relevant for material models comprising the kinematic hardening component. It also depends on stress state, being more relevant for plane strain state, as is the case [116]. The numerical model comprises both conditions, thus this effect is expected to be relevant, causing the crack closure to eventually cease. Even if the crack closure remains higher for the model with the GTN, the protection to the material is reduced approaching it to the levels showed by the model without GTN. As the protection decays the higher tendency to accumulate plastic strain, due to the deterioration of the material through porosity, comes on top. Crack closure is therefore the key to understand the *da/dN* behaviour of both models.

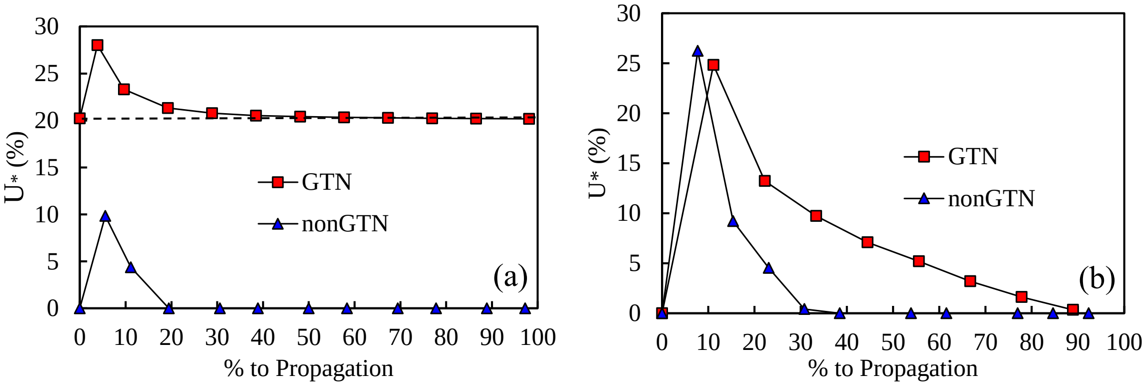

Figure 5.6. Crack closure level with and without GTN **(a)** a_0=11.5 mm, between the 25th and 26th crack propagations. **(b)** a_0=21.5 mm, between the 36th and 37th crack propagations. The results are presented in percentage up to propagation.

Finally, crack closure was disabled in the model with GTN. This is achieved numerically by deactivating the contact of the nodes that cover the crack flanks. Figure 5.7a presents the plastic strain evolution, throughout the time period between the 25th and 26th propagations, for the two specifications of the model with GTN – with and without contact – for a_0=11.5 mm. Figure 5.7b presents analogous results but for the plastic strain build-up at the single load cycle, immediately before the 26th propagation. Figure 5.7a shows that the plastic strain starts from similar levels after the 25th node release. The subsequent increase of plastic strain is much faster without crack closure. Thus, the *da/dN* differences are only consequence of the much faster accumulation of plastic strain. Figure 5.7b shows that plastic strain starts to rise much sooner without crack closure. In other words, crack closure delays the start of the accumulation of plastic strain at each loading cycle. This means that the contact of the crack flanks reduces the range of effective stress at the crack tip. Since the plastic strain is a nonlinear entity, during the growing stage it follows a nonlinear trend. Nevertheless, this trend is essentially the same for both variations of the model, as indicated by the dashed lines in figure 5.7. With crack closure, as its start is delayed, when maximum force is achieved the accumulation is just at a different stage of the same path. The same trend is followed during the unloading phase. However, crack closure influences the last part of the loading cycle, planning the accumulation of plastic strain.

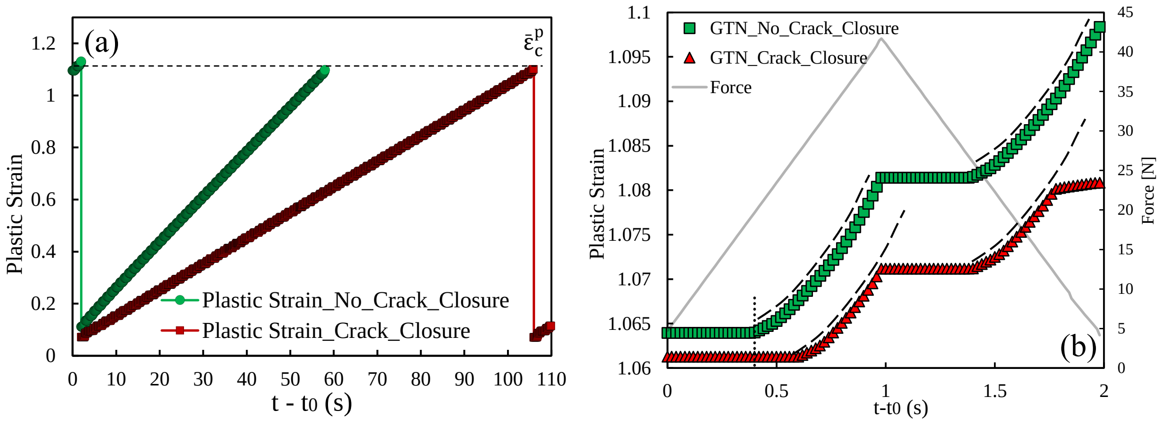

Figure 5.7. Effect of crack closure on plastic strain evolution, for a_0 = 11.5 mm. **(a)** Period between the 25th and the 26th crack propagations; **(b)** A single load cycle, before the 26th crack propagation.

Figure 5.8 shows *da/dN-ΔK* results for the model considering GTN model, with and without crack closure, in log-log scales. The models without crack closure produce higher values of *da/dN*, which is according to the result in Figure 5.7. The dramatic effect of disabling crack closure for a_0=11.5 mm is attenuated for a_0=21.5 mm. As discussed before, the effect of crack closure is of less importance for a_0=21.5 mm. Thus, for higher values of ΔK, the FCG rate with and without crack closure would be very close, as show in Figure 5.8.

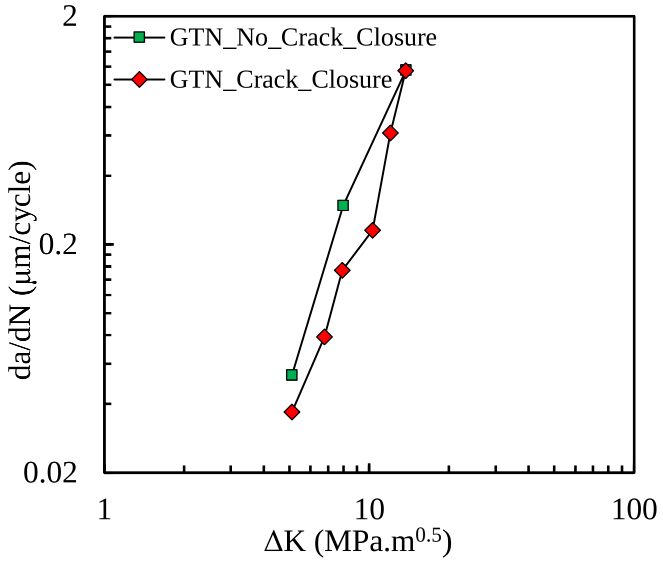

Figure 5.8. Effect of crack closure on *da/dN* values (model with GTN).

5.1.5. Comparison with Experimental Data

Past simulations of *da/dN* were based solely on the plastic deformation as a driving force, which is independent on mean stress. The inclusion of the nucleation and growth of microvoids is a step towards a better understanding of FCG. In fact, the existence of intrinsic defects may be expected, resulting from technological processes like casting or additive manufacturing. Besides, voids nucleate by debonding of the second phase particles.

Figure 5.9 compares experimental results of *da/dN* with numerical predictions obtained with and without the GTN model. Negleting the inclusion of the growth of microvoids, the numerical model underestimates the slope of *da/dN*-Δ*K* curve in log-log scales. With GTN there is an anti-clockwise rotation of the curve approximating it to the experimental results. Note that the Paris-Erdogan law m parameter is 3.62 in the experimental results, which is still higher than the ones obtained with GTN (m=3.37) and without GTN (m=2.61). However, the model with GTN provides a slope closer to the experimental one.

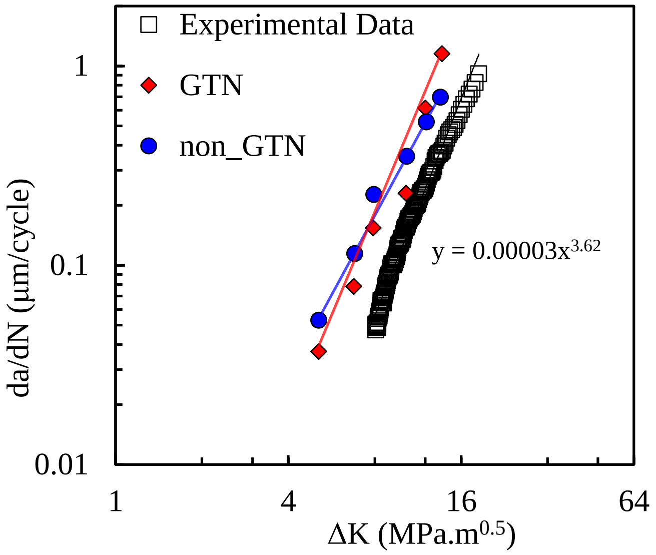

Figure 5.9. *da/dN-ΔK* curves in log-log scale (plane strain; F_{min} = 4.17 N; F_{max} = 41.7 N; R = 0.1). The Paris-Erdogan law parameters are shown on the equation related to the trend-line added to the experimental results.

5.2. Porosity, Plastic Strain and Stress Triaxiality Relation

The plastic strain arising at the crack tip leads to an accumulation of damage defined in terms of porosity growth. In other words, the plastic strain is the driving force of porosity accumulation. Thus, the implementation of the GTN model, in the existing FCG model, was expected to result in a growth of damage in accordance with the evolution of plastic strain at the crack tip. To verify this relation, both entities were analysed at the crack tip node. Figure 5.10 shows the evolution of porosity with the plastic strain, during all load cycles of a single propagation, for three different values of initial crack length, namely 5, 11.5 and 21.5 mm. Note that the results are presented in natural scales. There is a general trend for the increase of porosity with plastic strain. For a_0= 5 mm there is an initial non linear increase in porosity, followed by a saturation zone. This means that the plastic strain increases but the porosity does not increase. In the case of a_0=11.5 mm, the initial non linear increase is followed by a linear increase of porosity with the plastic strain. For a_0=21.5 mm there is neither initial transient regime nor saturation. The maximum porosity is near 0.045, i.e., 4.5% of the material volume is composed by voids when the plastic strain is of about 110%, for a_0=21.5 mm.

The increase of the initial crack length tends to increase the porosity growth rate, which means that for the same plastic strain there is more porosity. The higher initial crack lengths induce higher Δ*K* values, which result in higher porosity levels at the instant of node release. The values of porosity at the beginning of each increment also depend on initial crack length. Note that the numerical model works with a discrete propagation scheme: at the critical plastic strain the node containing the crack tip is released. Thus, when propagation occurs, the crack tip advances, moving away from the highly strained zone. Using the TPS approach, the plastic strain and porosity occurring at the node immediately ahead of the crack tip is the starting point when propagation occurs. However, this change on the node containing the crack-tip leads to sudden changes in the values of the variables under analysis. For a_0=21.5 mm, both plastic strain and porosity are higher than for the remaining initial crack lengths. On its way, for a_0=11.5 mm, only porosity is set to higher level than for the lower initial crack length. This occurs because higher stress intensity factors result in higher plastically affected zones, and higher strains. This way, when crack advances it reaches differently affected zones explaining the obtained values of porosity and plastic strain. The successive load cycles cause the porosity to gradually grow. Therefore, the premise that the build-up of plastic strain causes an accumulation of plastic damage is verified.

Another interesting detail perceptible in Figure 5.10 is the fact that porosity shows an oscillating behaviour. This is more perceptible for a_0=21.5 mm, due to the higher oscillation's amplitude, but it also occurs for the remaining values of $a_{0.}$ During the unloading phase of each loading cycle, the stress verified at the crack tip is of compressive nature. This stress causes the micro voids on the material to partially close and consequently the porosity is reduced. Nevertheless, the micro-cavities do not disappear since the damage is irreversible.

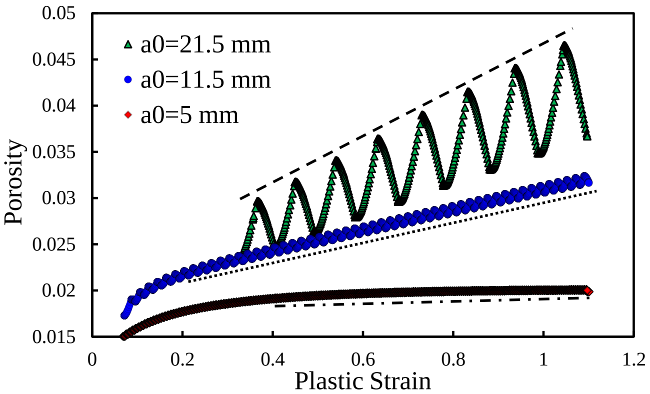

Figure 5.10. Porosity evolution with plastic strain growth for different initial crack lengths (a_0) in natural scales. Crack closure is enabled.

The differences in the evolution of the porosity with the plastic strain can be explained by the stress triaxiality at the crack tip. Indeed, using the GTN damage model, the void fraction evolution is significative affected by the stress triaxiality [117]. The present model only considers the growth of micro voids, being this process highly influenced by the stress triaxiality [67]. Figure 5.11a presents the evolution of the stress triaxiality at the crack tip during the propagation shown in Figure 5.2, comparing three different crack lengths. Figure 5.11b presents analogous results but for the porosity evolution. The horizontal axis denotes the progress up to propagation making possible to compare propagations with different lengths of time. Both results (stress triaxiality and porosity) were predicted at the maximum load instant. Globally, higher ΔK generate higher porosity levels, as highlighted in fig 5.11b. However, the stress triaxiality is initially very high for a_0=5 mm, generating a fast increase in porosity, as shown in Figure 5.11b. Then, stress triaxiality stabilizes, which is coinciding with the saturation of porosity. Comparing with the lower crack length, for a_0=11.5 mm the stress triaxiality is lower at the beginning, corresponding to a less abrupt increase in porosity. Also, stress triaxiality suffers a much less significant drop, which can explain the inexistence of stabilization on the porosity for this a_0. For the higher initial crack length, the stress triaxiality is relatively high, presenting a slight increase during the propagation, which leads to the higher slope attained for porosity.

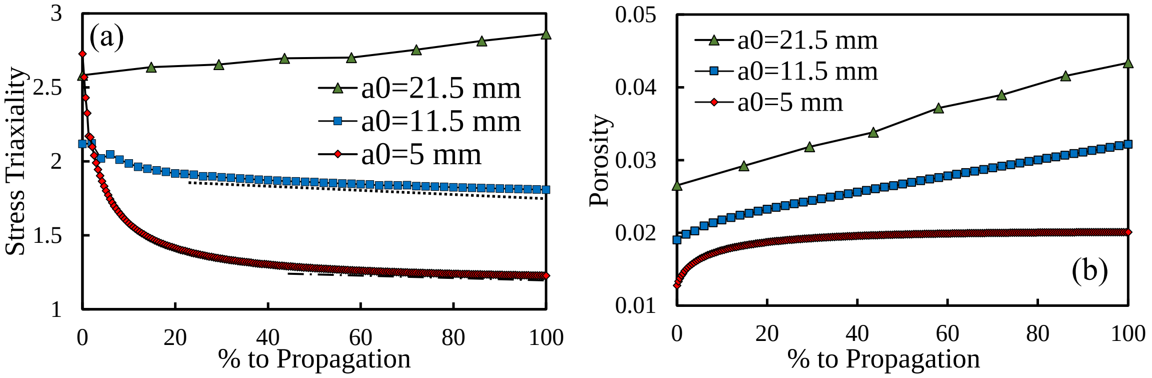

Figure 5.11. **(a)** Stress triaxiality throughout the entire propagation studied in Figure 5.2. **(b)** Porosity evolution for the same propagation.

5.3. Influence of Each GTN Parameter on FCG

5.3.1. Effect of Initial Void Volume Fraction, f_0

The initial void volume fraction, f_0, represents the fraction of material volume, in terms of cells, that is composed by voids a priori. Note that assuming positive f_0 imposes the existence of defects innate to the material. Moreover, if the nucleation process is disabled, as it is the case, the damage evolution is represented only by the growth of the pre-existing micro-voids. The primordial step to understand the influence of the different GTN parameters on the porosity, plastic strain and, consequentially, fatigue crack growth rate, is to understand the effect of the pre-existing voids. Therefore, *da/dN* was studied for two different crack lengths: a_0=11.5 mm and a_0=19 mm, which will lead to different ΔK values. Figure 5.12 shows the da/dN values, in natural scales, for the two initial crack lengths in terms of four different initial porosities: 0.005, 0.01, 0.02 and 0.03. All the values were obtained regarding the same propagation, at the stable FCG zone, i.e., after the initial transient regime associated with the stabilization of cyclic plastic deformation and formation of residual plastic wake. For a_0=19 mm there is a clear influence of the initial porosity on the *da/dN*. Moreover, it was expected that a higher initial porosity would lead to higher plastic strain levels, and this way, higher propagation rates. However, the results follow the opposite trend, i.e., for lower initial porosities the propagation rate is higher, stabilizing for higher levels of porosity as show by the horizontal dotted line. A similar trend is followed for a_0=11.5 mm, but in this case the difference is much smaller. The stabilization in *da/dN* also occurs sooner. Crack closure was disabled for a_0=11.5 mm to identify the effect of this mechanism on *da/dN*. Results show that in the absence of crack closure the *da/dN* rises, in an approximately linear fashion, with f_0, as the dotted line indicates. However, the crack closure is a crucial mechanism in FCG since it is always physically present. Thus, it will be considered in the analysis of the following parameters.

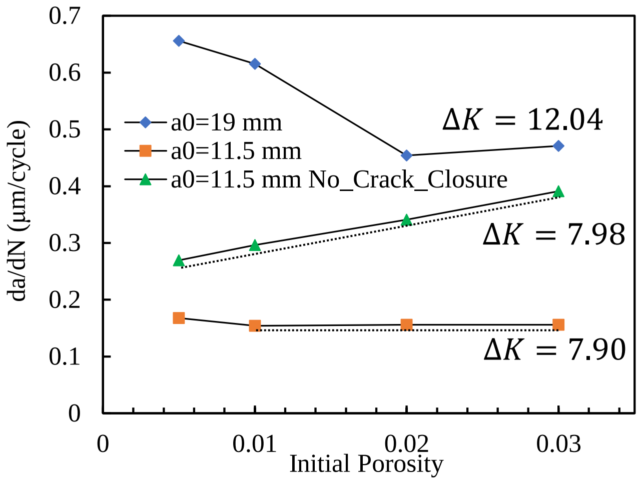

Figure 5.12 Fatigue crack growth rate in terms of the initial porosity for two distinct crack lengths (a_0=11.5 mm and a_0=19 mm). Results are shown in natural scales. Nucleation and coalescence are disabled (*q_1=1.5, q_2=1, q_3=2.25. F_{max}=41.67, F_{min}=4.17, R=0.1,* plane strain state).

To explain the unexpected behaviour observed in Figure 5.12, the porosity evolution was studied, in terms of the plastic strain build-up through the load cycles between the 24th and 25th propagation, for all the porosity values on the two distinct crack lengths. Figure 5.13a shows the referred results for a_0=11.5 mm, while Figure 5.13b presents analogous data for a_0=19 mm. The porosity at the beginning of a propagation is higher for higher values of f_0. On the other hand, the slope of the curves is slightly higher for lower values of f_0 . However, some saturation occurs for $f_0 = 0.02$ and $f_0 = 0.03$,i.e., the initial increase on porosity is higher, but on the latter part of the propagation the void growth mechanism saturates. For a_0=19 mm, the porosity at the beginning of the propagation also rises with the initial porosity. However, the trends followed for the different values of f_0 are distinct to the ones verified for a_0=11.5 mm: here higher values of initial porosity led to higher porosity accumulation rate at the end of the propagation. Thus, two conclusions may be drawn. Firstly, the initial porosity affects the growth of the micro-voids. Secondly, no saturation on the porosity occurs for this initial crack length, due to the higher levels of ΔK at the crack tip. Additionally, the porosity variations between the two stages of the load cycles are much more relevant for a_0=19 mm and the slopes are higher for this crack length too, which is also explainable due to the higher ΔK. Although higher values of f_0 lead to higher porosity levels, the gap between the curves is not proportional to the difference between the initial porosities. Thus, other mechanisms need to be involved in the process.

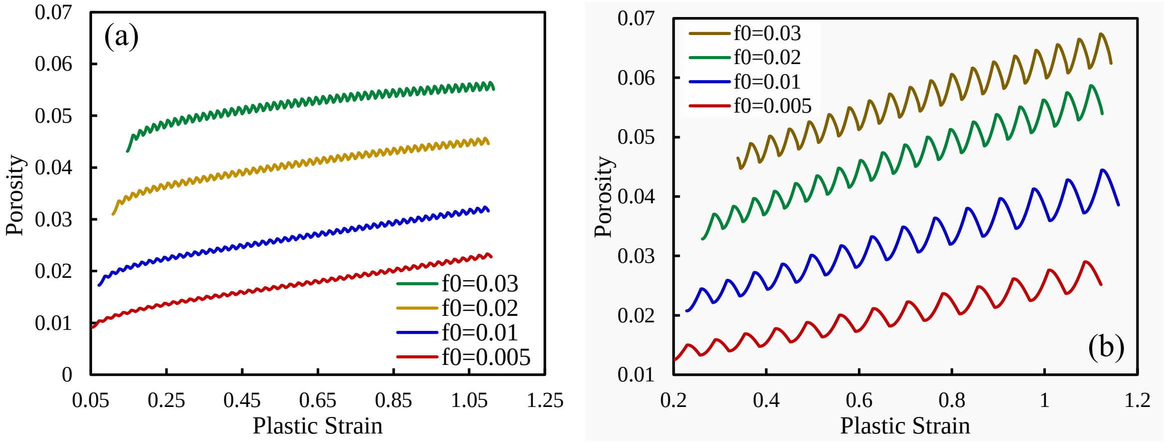

Figure 5.13. Porosity growth due to the accumulation of plastic strain for distinct values of f_0 for: **(a)** a_0=11.5 mm and **(b)** a_0=19 mm. Results are shown in natural scales.

The evolution of the porosity is directly influenced by the material parameters adopted in the GTN model. The adopted numerical model considers plastic strain to determine the crack propagation. Thus, this is the entity studied to explain the *da/dN* values shown previously. Figure 5.14 presents the plastic strain build-up in terms of pseudo-time. Note that, similarly to the results presented in section 5.1.2, the instants presented on the scale are relative to the beginning of the new propagation. The time was reset to allow the comparison of the 25th propagation for different values of initial porosity, which due to the *da/dN* differences occurs at different instants of the simulation. Results are shown in natural scales. Figure 5.14a is relative to a_0=11.5 mm and Figure 5.14b to a_0=19 mm. For the first initial crack length, plastic strain grows inside a narrow band delimited by the dashed lines, which explains the similar results of *da/dN* for the different values of f_0 (see Figure 5.12). Note that the plastic strain accumulation is slightly faster for the lower initial porosity, in comparison with other curves, which is in accordance with the *da/dN* results. Additionally, higher f_0 values result in higher plastic strains at the beginning of the propagation, which agrees with the porosity outcomes. For a_0=19 mm the plastic strain at the beginning of the propagation also increases with f_0, but the values are globally much higher for this initial crack length. The porosity levels are distinct for both initial crack lengths due to ΔK differences. Regarding the larger value of crack length, curves can be grouped in two groups: $f_0 = 0.005$ and $f_0 = 0.01$, which result in a faster, slightly linear, accumulation, in agreement with the faster *da/dN*; $f_0 = 0.02$ and $f_0 = 0.03$ lead to a slower, linear, plastic strain build-ups and propagation rates. This behaviour agrees with the predicted *da/dN* results shown in Figure 5.12. However, explaining the plastic strain trends is the major challenge as it will close the questions loop.

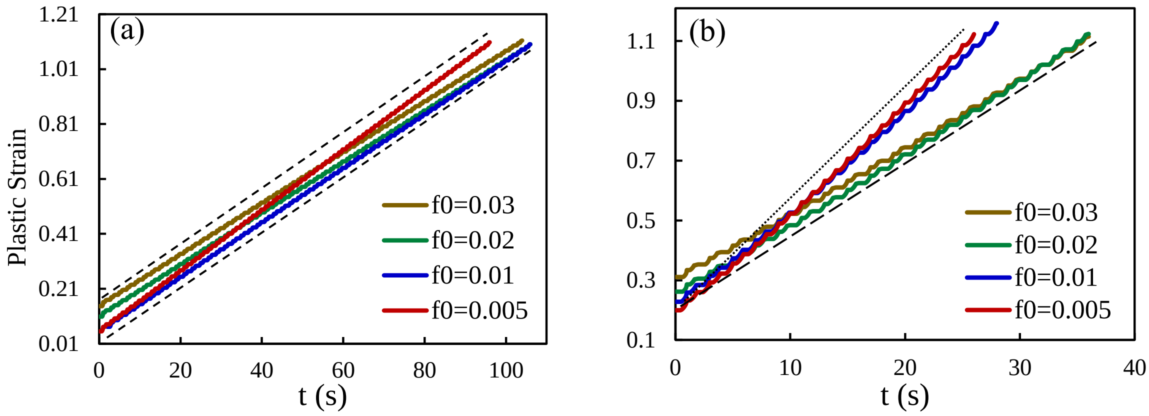

Figure 5.14. Plastic strain accumulation vs pseudo-time for the different values of f_0 for both crack lengths. **(a)** a_0=11.5 mm **(b)** a_0=19 mm

Crack closure is usually able to explain the trends followed by the plastic strain. Consequently, an analysis analogous to the ones discussed previously was performed at the node immediately behind the crack tip. Figure 5.15a presents the crack closure for a_0=11.5 mm while Figure 5.15b refers to a_0=19 mm. Again, crack closure is evaluated as a function of propagation fraction. For a_0=11.5 mm, the crack closure trend is different for each value of f_0 , explaining the differences in the plastic strain evolution. Thus, higher porosities and higher plastic strains generate higher levels of crack closure, which protects the material from the lower mechanical resistance conferred by the higher porosity, levelling the plastic strain accumulation. The lower level of crack closure for $f_0 = 0.005$ results in a faster plastic strain build-up and consequentially a higher *da/dN*. In the case of a_0=19 mm, two lowest values of f_0 suffer smaller deformations inducing lower levels of crack closure. Strain ratcheting also occurs, disabling the stabilization of crack closure. This allows a faster accumulation of plastic strain, especially for $f_0 = 0.005$, where crack closure completely ceases, explaining the higher propagation rates. The second group, with higher f_0 values, has a much higher crack closure. Consequentially the plastic strain accumulation is delayed resulting in lower levels of *da/dN*. Note that for this second group no strain ratcheting occurs. Thus, the disabling of this phenomenon must be related or with the higher f_0 or with the higher void growth rate experienced for higher values of f_0.

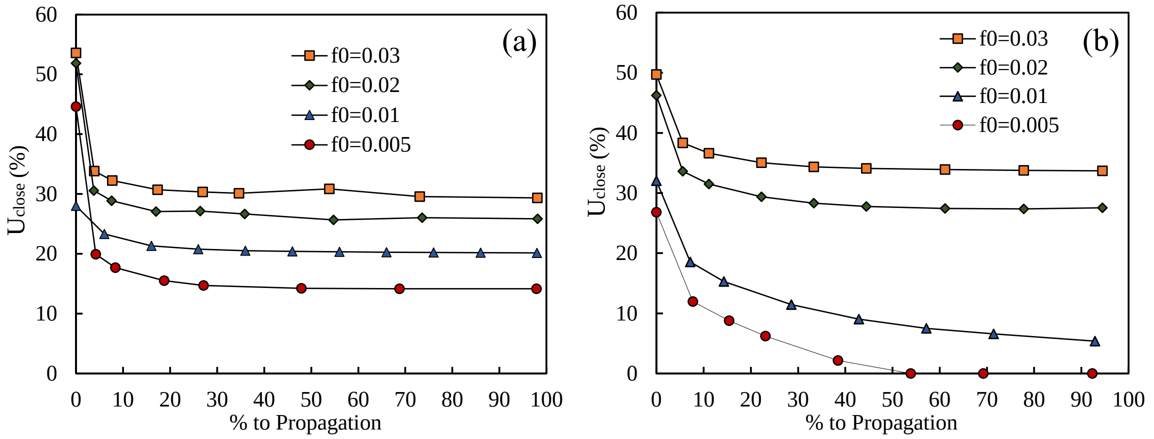

Figure 5.15. Crack closure level for: (a) a_0=11.5 mm (b) a_0=19 mm.

5.3.2. Effect of the Tvergaard Parameters, q_1, q_2 and q_3.

As referred, Tvergaard modified the Gurson's model to account for micro-void interactions adding three additional parameters: q_1, q_2 and q_3. Each one of these parameters as a specific effect on the growth of micro voids process. q_1 accounts for the loss of strength due to the interactions occurring between different voids, q_2 and q_3 influence the effect of the stress triaxiality and void volume fraction, respectively, on the plastic potential. Tvergaard proposed standard values for these parameters that are widely used (q_1=1.5, q_2=1, q_3=2.25). However, to not disregard the importance of these parameters they were also included in the sensitivity analysis. The effect of these parameters on the predicted *da/dN* is shown in Figure 5.16. Each curve represents one of the parameters and the results are presented in natural scales. The loading case is the same applied in the study of f_0.

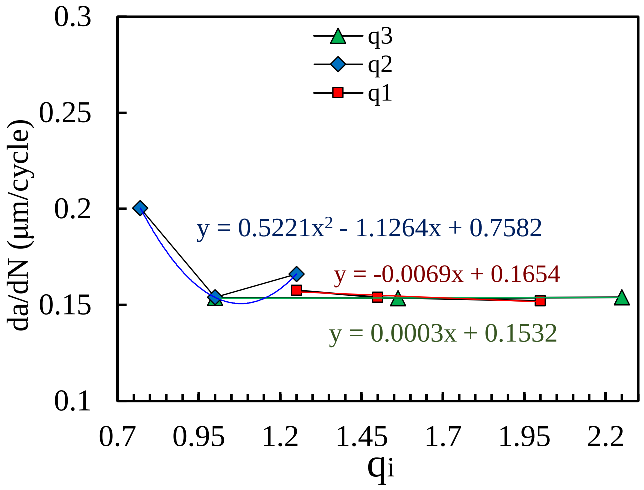

Figure 5.16. *da/dN* in terms of each Tvergaard parameter for a_0=11.5 mm. Results are shown in natural scales. Nucleation and coalescence are disabled. When q_1 is changed: q_2=1 and q_3=2.25. When q_2 is changed: q_1=1.5 and q_3=2.25. When q_3 is changed: q_1=1.5 and q_2=1. (f_0= 0.01).

5.3.2.1. Analysis of q_1

Results presented in Figure 5.16 show that the variation of q_1 has little effect on the FCG rate as the low slope of the trend line as evidences. This means that the build-up of plastic strain is similar for all values of q_1. However, this fact does not mean that porosity follows the same trends. These two variables were studied on the node containing the crack tip. Figure 5.17a presents the plastic strain evolution, while Figure 5.17b contains the porosity evolution. The plastic strain build ups are almost overlapped, for the three distinct values of q_1, explaining the similar *da/dN* values. Nevertheless, the overall porosity level increases with q_1. This increase in porosity occurs due to two conditions: higher porosities at the beginning of the new propagation, and higher slopes of the porosity build-up, during the propagation. Thus, raising q_1 results in a harsher loss of strength of the material, which manifests itself by an increase in porosity. However, this effect is not as intense as the one verified for f_0. Indeed, in the presence of crack closure, the plastic strain build-up ends up being unchanged leading to similar values of *da/dN*.

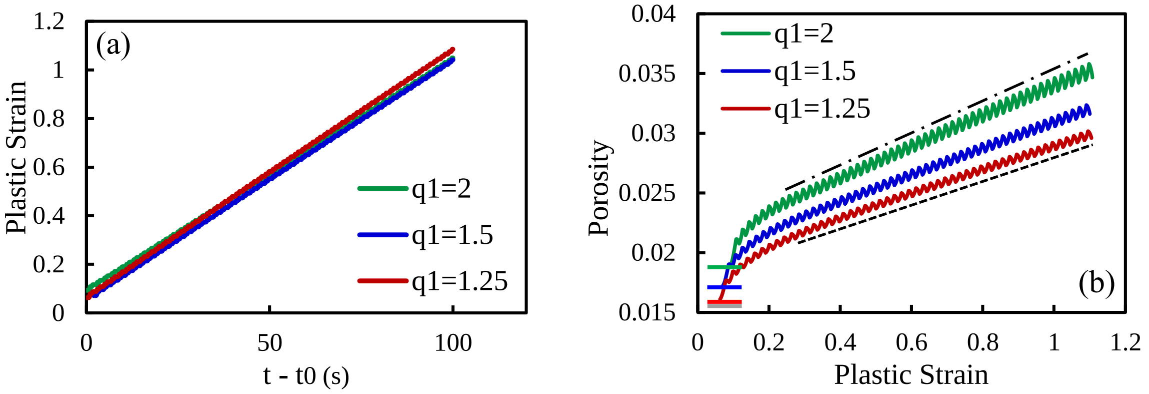

Figure 5.17. (a) Plastic strain evolution for distinct values of q_1. The q_1=2 curve is almost indistinguishable because it is overlapped by the others. **(b)** Porosity evolution due to the increase in plastic strain. Results are shown in natural scales.

5.3.2.2. Analysis of q_2

The *da/dN* values obtained for three distinct values of q_2 parameter (0.77; 1 and 1.25) are shown in Figure 5.16. There is no linear relation between q_2 and *da/dN*, the higher FCG rate is attained for q_2=0.77, there is a minimum in the propagation rate for q_2=1 and then an intermediate value for q_2=1.25. This trend indicates that another mechanism may be influencing the fatigue crack growth. Empirically, from previous results, one is expecting that crack closure is the responsible for the registered variations. Figure 5.18a presents the plastic strain accumulation for the studied values of q_2. The results agree with the *da/dN* values and with the expectation that crack closure has a main role in the process. The smaller value of q_2 has a lower initial plastic strain, i.e., after the previous propagation occurred. However, the higher plastic strain accumulation rate, evidenced by the higher slope of the respective curve, balances this fact resulting in the faster propagation rate. Note that for q_2=1 and q_2=1.25 the plastic strain accumulation rate is similar. However, as a higher initial plastic strain arises for q_2=1.25 the *da/dN* ends up being higher. Figure 5.18b presents the porosity evolution as a function of the plastic strain, for the previous values of q_2. As expected, higher q_2 values are translated in higher porosities. However, the relation between the initial plastic strain is not linearly coincident with the initial porosity, i.e., only the higher value of q_2 has a higher initial plastic strain. Note that even if the higher porosity leads to the higher initial plastic strain, this entity is very similar for the remaining values of q_2 despite the notorious difference in the porosity level. Overall, the porosity trends are similar: there is a harsher initial increase followed by a linear evolution with a lower slope. The slopes are different for the different q_2 values being the initial disparity preserved during the propagation. Thus, higher values of q_2 result in higher values of porosity, but not necessarily higher *da/dN*.

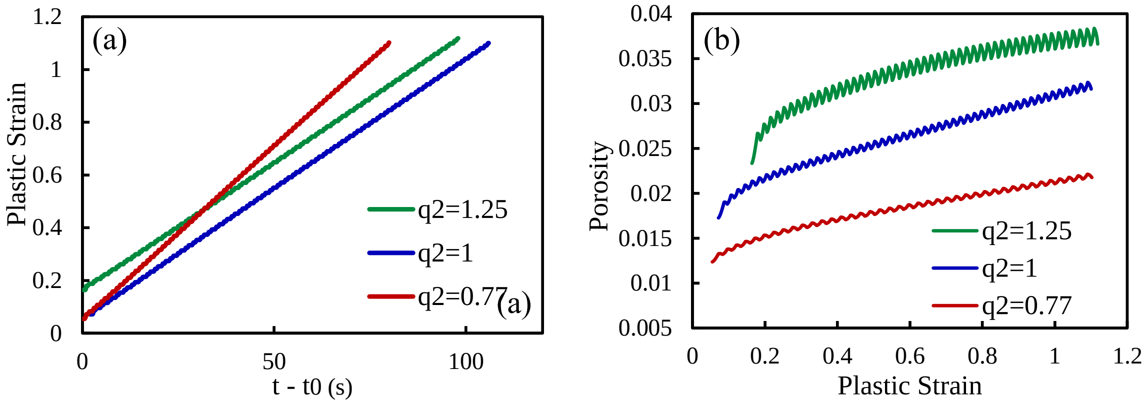

Figure 5.18. (a) Plastic strain evolution in terms of the distinct values of q_2. **(b)** Porosity evolution, due to the increase in plastic strain, for the same values of q_2 previously referred. Results are shown in natural scales.

In order to verify the hypothesis that crack closure has a key role in the process, affecting the attained crack propagation rates, the crack closure was studied during the propagation (see Figure 5.19). The trends are once again similar for all the values of the studied parameter as there is a stabilization after an initial peak in crack closure. The higher initial plastic strain, for q_2=1.25, results in an initial higher crack closure. After stabilizing the maximum value of crack closure is still reached for q_2=1.25, but close to the one attained for q_2=1. This agrees with the similar slopes registered by the plastic strain accumulation (see figure 5.18a) for these two values. Note that the slope is slightly lower for the higher value of q_2, agreeing with the higher crack closure levels attained. The lower value in crack closure is obtained for q_2=0.77. As the protective fashion induced by this entity is lesser, the plastic strain accumulation is faster resulting in a higher *da/dN*. In conclusion, higher porosities result in higher crack closure levels which, consequentially, influences *da/dN* explaining the plastic strain trends and *da/dN* predictions.

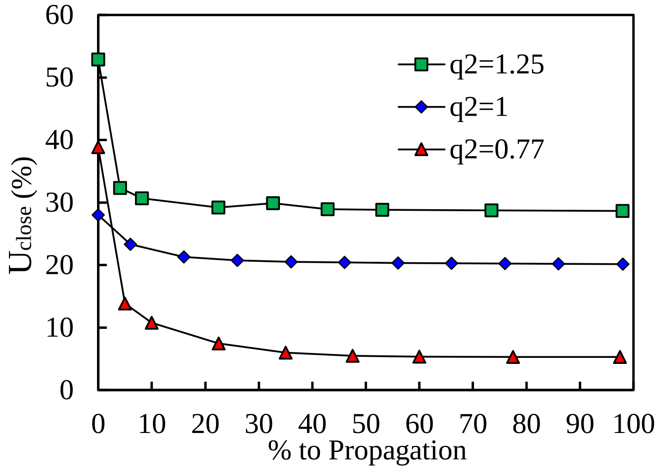

Figure 5.19. Crack closure level for distinct values of *q₂*. Results are presented in terms of the percentage of load cycles completed to the load cycles needed to propagation to occur.

5.3.2.3. Analysis of q_3

The da/dN predictions shown in Figure 5.16 demonstrate that the q_3 parameter has little effect on the FCG rate. The slope of the trend line added to the results is almost null. To support this result, the plastic strain accumulation was studied on the node containing the crack tip. The obtained results are presented in Figure 5.20a. In fact, the curves are almost overlapped agreeing with the *da/dN*. The porosity evolution is presented in Figure 5.20b. The curves are also overlapped, which explains the similarity in the plastic strain accumulation.

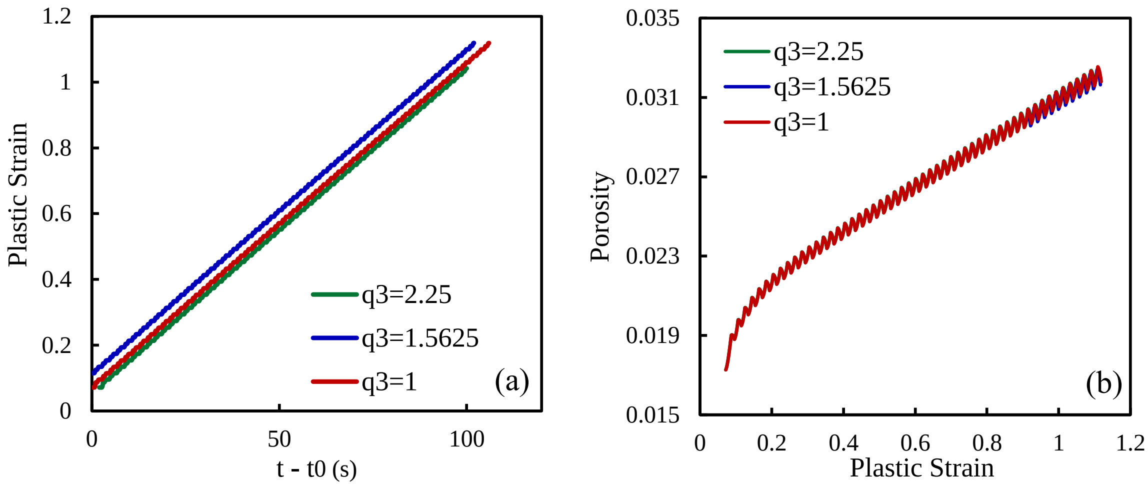

Figure 5.20. (a) Plastic strain evolution in terms of the distinct values of q_3. **(b)** Porosity evolution, due to the increase in plastic strain, for the same values of q_3 previously referred. Results are shown in natural scales.

5.3.3. Effect of the Void Fraction to be Nucleated, f_N

The void fraction to be nucleated by means of plastic strain rate, f_{N}, influences the nucleation process by means of Equation (3.10). This parameter is related to the voids nucleated by debonding of the second phase particles, in this case, with dependence on the history of plastic strain. The physical meaning of this numeric parameter is that a total fraction, equal to f_{N}, of new voids may be nucleated due to plastic strain.

Figure 5.21 presents the *da/dN* in terms of different values of f_{N} in: (a) log-log scales for $f_{\mathrm{N}} = \{0.001; 0.01; 0.1\}$ and (b) natural scales for $f_{\mathrm{N}} = \{0; 0.001; 0.01; 0.1\}$. These values were selected taking into account the common range of values for this aluminium alloy (0.001 to 0.1) [97]. The natural scales were introduced to allow the presentation of the point attained for $f_{\mathrm{N}} = 0$. This value of f_{N} means that no void nucleation occurs due to plastic strain history. Simulations were performed on an initial crack length of 11.5 mm, which leads to average levels of ΔK (≈ 7.9 MPa.m$^{0.5}$), sitting in the Paris-Erdogan regime of a *da/dN*-ΔK curve. In log-log scales the curve is not linear (see Figure 5.21), a small increase in *da/dN* is achieved from 0.001 to 0.01, which was expected since the porosity to be nucleated is smaller or of the magnitude of the considered initial porosity ($f_0 = 0.01$). *da/dN* is then almost doubled when the porosity to be nucleated reaches an order of magnitude higher than f_0. In natural scales there is an initial increment when nucleation is activated and then the curve stabilizes in a linear trend. These results show that unlike the increase in f_0, the activation of the nucleation process, and the increase on the nucleated porosity, rise *da/dN*. Such results suggest that nucleation interferes on the crack closure.

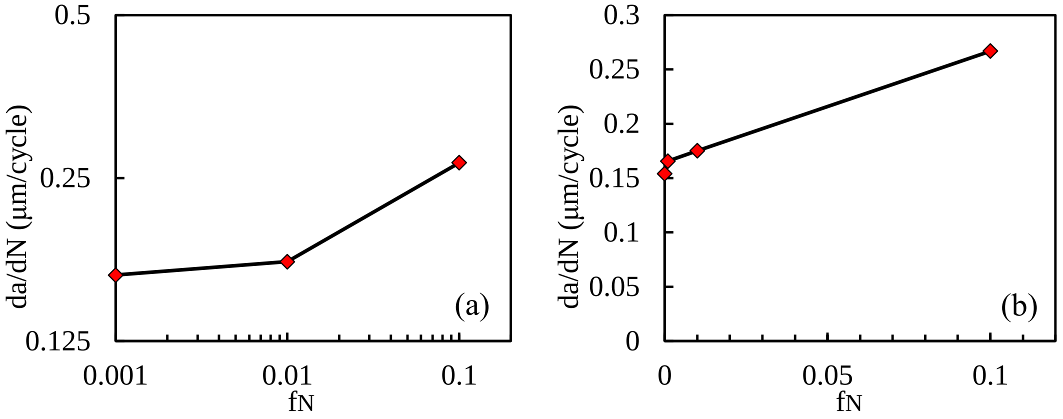

Figure 5.21. *da/dN* in terms of f_{N}, for an initial crack length of 11.5 mm in: **(a)** log-log scales; **(b)** natural scales. Coalescence is disabled (q_1=1.5, q_2=1, q_3=2.25, f_0=0.01, ε_{N} =0.25 and s_{N}=0.1).

To understand the influence of the nucleation process on the predicted *da/dN* it is crucial to analyse the porosity and plastic strain evolutions. These entities are proven to highly influence crack closure and *da/dN* itself. Figure 5.22a shows the plastic strain evolution for the same entire propagation, in terms of pseudo-time, for the different values of f_N . Note that alike Figure 5.13a an entire propagation is shown. Figure 5.22b presents the porosity evolution with plastic strain build-up for the same entire propagations, previously referred. Porosity is shown in logarithmic scale due to the different orders of magnitude achieved. The increase on the fraction of porosity to be nucleated causes an increase on the plastic strain at the beginning of the propagation. The inclusion of the nucleation process accelerates the build-up of plastic strain, explaining the increase in *da/dN*. Moreover, a small nucleation amplitude ($f_\mathrm{N} = 0.001$) results in a small increase in the accumulation speed of plastic strain, coinciding with the small increment witnessed in natural scales. The plastic strain trend keeps almost linear until the order of magnitude of the initial porosity is reached. For the higher value, a quadratic behaviour is followed, explaining the slope increase in log-log scales. Nucleation was set to occur around a plastic strain of 0.25 (ε_N =0.25) - marked with a vertical dashed line on Figure 5.22b. The nucleation process does not change the initial trend followed by porosity. Also, the porosity evolution is never completely linear, and it tends to saturate. Saturation occurs latter and is more prominent for higher values of f_N. Overall, the porosity level increases with the growth of the nucleation amplitude, validating its effect. Additionally, it does not seem to influence the growth of micro-voids process. Note that for $f_\mathrm{N} = 0$ the increase in porosity is about $\Delta f_\text{void growth} = 0.015$, which must be due to the growth of micro-voids. Using $f_\mathrm{N} = 0.01$ the overall increase in porosity is about $\Delta f_\text{total} = 0.025$. Although a fraction is related to the nucleation process ($\Delta f_\text{Nucleation} = 0.01$), the remaining part is linked to the void growth process $\Delta f_\text{Void Growth} = 0.015$, which is the same that was attained when no nucleation occurred.

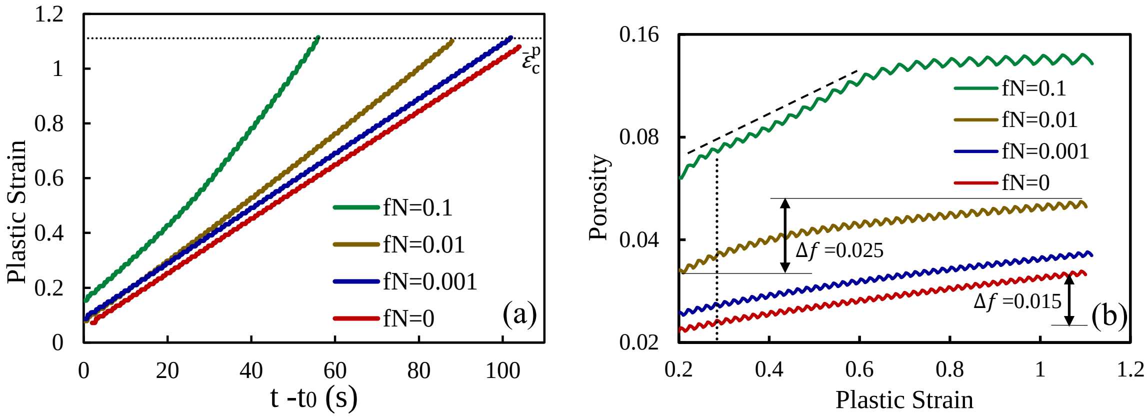

Figure 5.22. (a) Evolution of plastic strain for the same entire propagation depending on the f_N value. **(b)** Evolution of porosity in terms of plastic strain for the different values of f_N, porosity is in logarithmic scale.

Crack closure was studied for the same propagation presented in Figure 5.22, considering different values of f_N (see Figure 5.23). The crack closure evolution is almost independent of f_N. The trend is similar for all the values of the nucleation amplitude: there is an initial peak followed by a fast stabilization of crack closure. Note that the curve for $f_N = 0.001$ is very close to the curve without nucleation which is in accordance with the previous results. Crack closure is higher for $f_N = 0.01$, which was also expected due to the higher levels of plastic strain occurring at the crack tip. However, it seems to occur a saturation for $f_N = 0.1$ as the significantly higher level of plastic strain does not result in a higher crack closure.

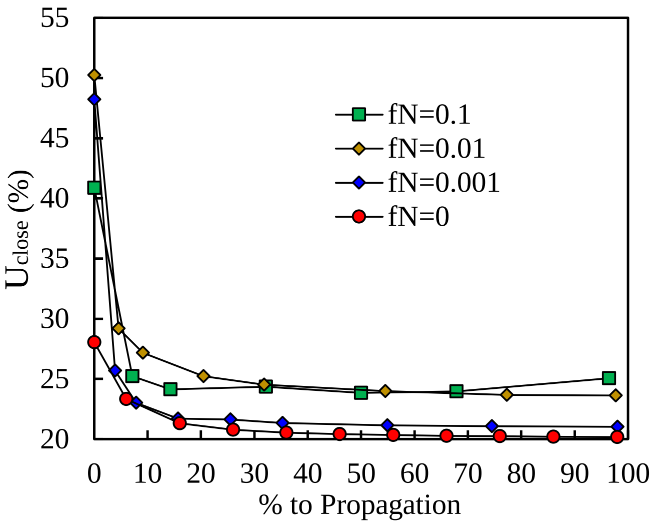

Figure 5.23. Crack closure through the same propagation studied in Figure 5.11.

5.3.4. Effect of the Mean Nucleation Strain, ε_N

Chu and Needleman [42] idealized that nucleation occurs due to a mean plastic strain, ε_N. The nucleation strain is distributed in a Gaussian fashion around that mean. Since this distribution is affected by a standard deviation, the nucleation may occur either before or after the mean nucleation strain. This parameter is expected to affect the porosity distribution through the load cycles of each propagation. Figure 5.24 presents the *da/dN* values, in natural scales, for a crack with an initial length of 11.5 mm, in terms of four distinct ε_N values: 0.15, 0.25, 0.35 and 0.5. Results show that the effect of this parameter in terms of *da/dN* is negligible.

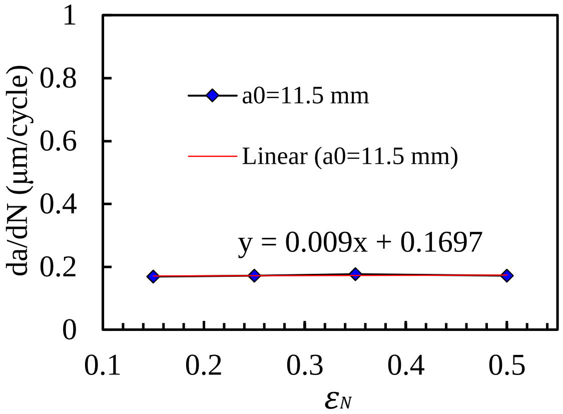

Figure 5.24. *da/dN* in terms of different values of ε_N. Results are presented in natural scales. Coalescence is disabled, $q_1=1.5$, $q_2=1$, $q_3=2.25$, $f_0=0.01$, $f_N=0.01$ and $s_N=0.1$.

Porosity and plastic strain were analysed in the node located at the crack tip, with the intent to explain the observed *da/dN* trend. The plastic strain and porosity evolutions are presented in Figure 5.25 for a single propagation. The plastic strain at the beginning of the propagation is very similar for all the values of ε_N. Moreover, its evolution is almost linear and the slope variations are contained in a narrow range (delimited by the two dashed lines in Figure 5.25a) for the different values of the mean nucleation strain. This explains the maintenance of *da/dN* for the different values of ε_N. Additionally, the higher value of plastic strain at the beginning of the propagation is achieved for $\varepsilon_N = 0.15$, which is in accordance with higher value of porosity, at the same instant, registered in Figure 5.25b. Since the maximum porosity is reached for $\varepsilon_N = 0.5$, the second higher plastic strain accumulation rate is obtained for the same value of mean nucleation strain. Thus, the plastic strain results are in good agreement with the porosity ones. Figure 5.25b shows that at the beginning of the propagation, smaller values of ε_N lead to higher initial porosities. This is in accordance with the normal distribution concept. Note that a mean nucleation strain of $\varepsilon_\mathrm{N} = 0.15$ implies that the higher rate of nucleation should occur for a plastic strain of 0.15. Results show that, for this ε_N, porosity tend to increase significantly at the beginning of plastic strain accumulation, saturating for higher values of deformation – as it moves away from the nucleation mean strain. On the other hand, for $\varepsilon_\mathrm{N} = 0.5$, the normal distribution is centred with the range of plastic strains that were reached. Thus, the porosity evolution has a much more linear trend, as it can be seen by the dashed-pointed line. Also, for $\varepsilon_\mathrm{N} = 0.15$ the plastic strains covered are almost completely placed on the left side of the distribution, losing importance with the grow up of plastic strain. On the other hand, for $\varepsilon_\mathrm{N} = 0.5$, the plastic strain covers a much more important area of the normal distribution, explaining the higher levels of porosity obtained.

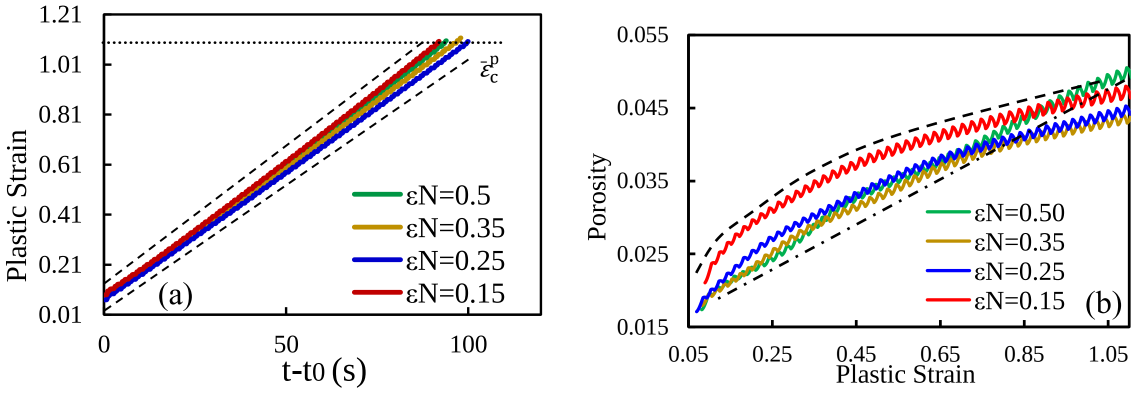

Figure 5.25. (a) Evolution of plastic strain for the same entire propagation depending on the ε_N value. **(b)** Evolution of porosity in terms of plastic strain for the different values of ε_N. All the results are in natural scales.

5.3.5. Influence of the Standard Deviation, s_N

Changing the standard deviation of the Gauss distribution allows to model different ranges of strain over which voids nucleate. Small standard deviations are supposed to cause the porosity to increase in a narrow strain range, while higher deviations should smooth the nucleation process in a wide range of strain. Also, narrow ranges of nucleation, caused by small values of s_N, were shown to have a destabilizing effect in the model [75]. To access the influence of these particularities on the fatigue crack growth rate, *da/dN* was calculated for different values of s_N: 0.01, 0.1 and 0.2. The result is presented in Figure 5.26 in natural scales for the same initial crack length: a_0=11.5 mm.

The influence of this parameter is small - *da/dN* is basically independent of s_N – as shown by the very small slope of the linear trend line. nevertheless, for $s_\mathrm{N} = 0.1$ *da/dN* is higher than for the two remaining values.

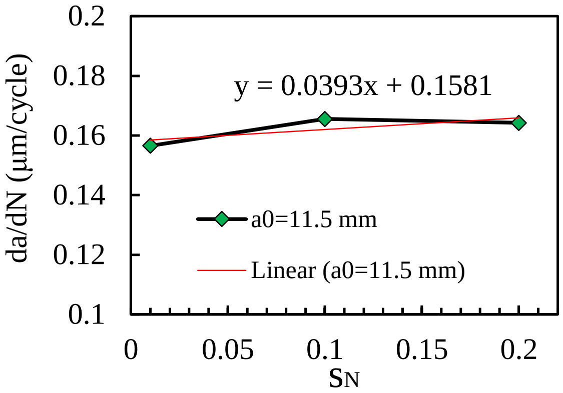

Figure 5.26. Effect of s_N on *da/dN*. Results are presented in natural scales for three distinct values of s_N: 0.01, 0.1 and 0.2. Coalescence is disabled, q_1=*1.5*, q_2=*1*, q_3=*2.2*5, f_0=0.01, f_N =0.01 and ε_N=0.25.

The plastic strain and porosity evolutions were obtained in the node located at the crack tip, comparing three values of s_N,. Results of plastic strain are presented in Figure 5.27a, for the same single propagation occurred at the end of the process, where *da/dN* has already stabilized. Analogous results, but this time for the porosity, are presented in Figure 5.27b. The plastic strain evolution explains the *da/dN* differences shown in Figure 5.26. The trends are similar, but faster accumulations occur for $s_\mathrm{N} = 0.1$ and $s_\mathrm{N} = 0.2$, which is in accordance with the faster propagation rates that were obtained. The standard deviation parameter affects essentially the porosity evolution, which should be able to explain the plastic strain trends. Figure 5.27b shows that the trends of the porosity are very distinct. The higher standard deviation results in the more linear trend. This was expected since nucleation occurs in a larger range of strains, reducing the porosity growth for each plastic strain increment. Obviously, that nucleation will eventually cease but this event is very smooth. For $s_\mathrm{N} = 0.1$ there is an initial linear increase in porosity until plastic strain reaches about 0.35. This is explained by the fact that nucleation occurs around $\varepsilon_\mathrm{N} = 0.25$ with a standard deviation of 0.1. After that, nucleation starts to decrease and porosity rises mainly due to the growth of micro voids resulting in a sort of saturation, as only one of the microvoids related processes remains active. This transition is less smooth as nucleation was more concentrated, resulting in higher increments of porosity. When this process ceases the slope of the curve for $s_\mathrm{N} = 0.1$ falls below the curve for $s_\mathrm{N} = 0.2$ as the last nucleation is still occurring. The higher initial increase in porosity results in a higher plastic strain level at the initial load cycles. The higher plastic strain then causes more porosity, like a snowball effect. This explains the overall higher porosity for this standard deviation. However, at the end of the propagation, the higher nucleation range for $s_\mathrm{N} = 0.2$ ends up offsetting the initial higher increase for $s_\mathrm{N} = 0.1$ resulting in a similar final porosity value (see Figure 5.27b).

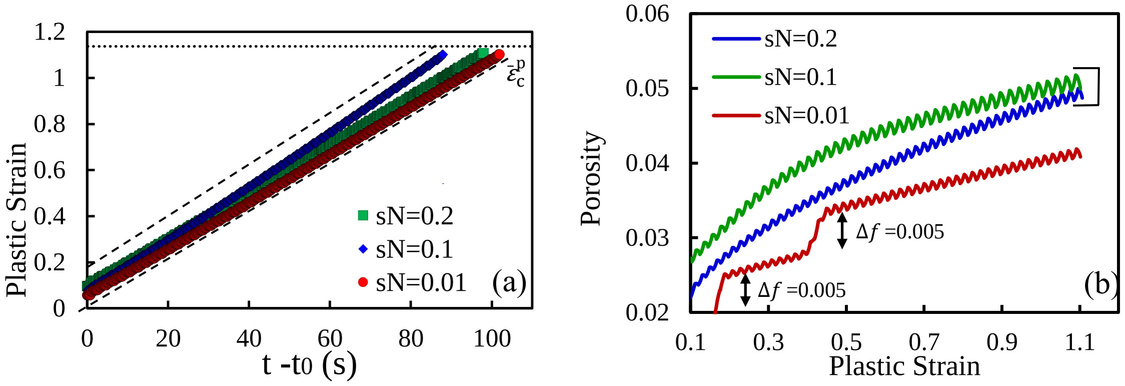

Figure 5.27. (a) Plastic Strain evolution throughout a single propagation for the three values of s_N. **(b).** Porosity build-up for the same propagations referred before. Results are presented in natural scales.

For $s_\mathrm{N} = 0.01$ the nucleation band is so narrow that porosity jumps. Note that porosity is computed at the Gauss points. Since this process has an instability effect, a smoothening operation is performed by considering the average in the two Gauss point closer to the node containing the crack tip. Therefore, two distinct jumps are captured in the process, one for each Gauss point considered in the average, since plastic strain increases at different trends in each Gauss point. Thus, when the average is computed the porosity rises half of the nucleation amplitude. Accordingly, the porosity was measured, in terms of plastic strain growth, for one of the Gauss points closer to the node located at the crack tip (Figure 5.28), considering $s_\mathrm{N} = 0.01$. In this case the increase in porosity, due to nucleation, is exactly the nucleation amplitude and only one jump is captured. However, a higher plastic strain is achieved at the end of the propagation because the crack propagates when a plastic strain of 110% is reached in the node, which is the average of the two Gauss Points. Thus, the plastic strain in the other Gauss point compensates the higher value reached in the one studied in Figure 5.28 and the average at the node will be of 110%.

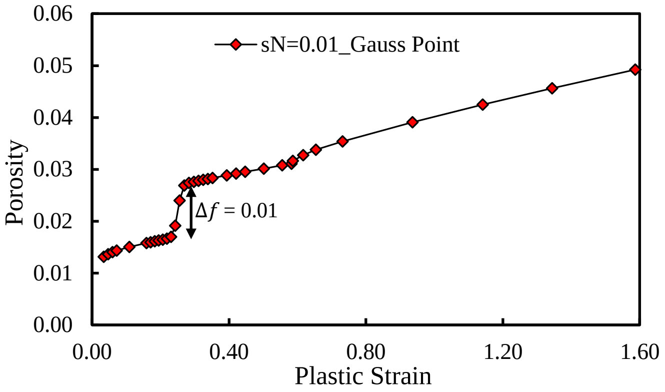

Figure 5.28. Porosity accumulation due to the occurrence of plastic strain at the Gauss point located immediately after the node containing the crack tip.

5.4. Sensitivity Analysis

In order to access the influence of each parameter previously studied on the predicted da/dN, a sensitivity analysis was carried out. This process allows to compare the variations on the output entities caused by different input parameters, with different physical dimensions.

The final output of a FCG oriented numerical model is the fatigue crack growth rate, expressed by *da/dN*. Thus, this is the target entity of the sensitivity analysis. The non-dimensional sensitivity of *da/dN*, to the selected GTN parameters is expressed as follows:

$$\nabla f = \frac{\partial \left(\frac{da}{dN}\right)_{\mathrm{p}}}{\partial m_{\mathrm{p}}} \cdot \frac{m_{\mathrm{p}}}{\left(\frac{da}{dN}\right)_{\mathrm{p}}}, \qquad (5.2)$$

where ∇f is the sensitivity coefficient and m_p represents the GTN material parameter. Each sensitivity coefficient represents the change rate of *da/dN* caused by a variation of a specific material parameter. Note that a sensitivity of 0.5 indicates that a variation of 1% in m_p produces a variation of 0.5% in $(da/dN)_{\mathrm{p}}$. The results obtained in the sensitivity analysis are presented in Figure 5.29. The sensitivity analysis was performed at the central point, or at one of the central points in the case where even number of values for the parameter were studied. Results show that q_2 parameter has by far the biggest influence on *da/dN*. q_1 is also important while q_3 has almost no influence. f_{N} is the nucleation related parameter with most importance, followed by ε_{N} and finally s_{N}. f_0 has also low importance.

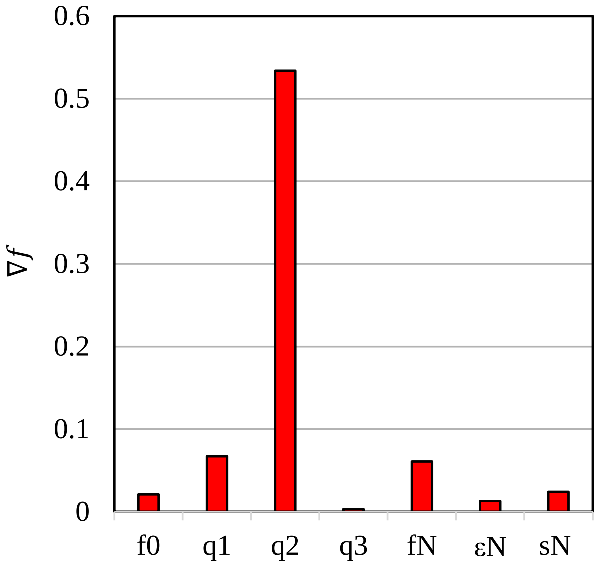

Figure 5.29. Sensitivity analysis carried out on the following parameters: $f_0 = 0.01$; $q_1 = 1.5$; $q_2 = 1$; $q_3 = 1.5625$; $f_\mathrm{N} = 0.01$; $\varepsilon_\mathrm{N} = 0.25$ and $s_\mathrm{N} = 0.1$.

6. CONCLUSIONS

The finite element method is adopted in the present study to analyse the fatigue crack growth. The numerical model assumes that cyclic plastic deformation at the crack tip is the FCG driving force. The growth of micro-voids was included in the analysis, providing a better modelling of crack tip damage. The influence of each GTN parameter on the FCGR was studied and used to perform a sensitivity analysis. The main conclusions are:

- The inclusion of micro-voids in the model based on cumulative plastic strain produced an unexpected decrease of *da/dN* for low values of ΔK. On the other hand, at relatively high values of ΔK, the GTN model increased the FCG rate.
- The inclusion of porosity in the analysis leads to an increase of the plastic deformation level, as well as the size of the plastic zones ahead of the crack tip.
- This higher plastic deformation results in higher plastic wakes at the crack flanks, increasing the crack closure level.
- At low values of ΔK, the inclusion of micro-voids increased plasticity induced crack closure (PICC), promoting the reduction of *da/dN*. At high values of ΔK, there is no PICC even with GTN. Therefore, the variations of *da/dN* are linked with changes of cyclic plastic deformation. Disabling the contact of crack flanks, results in an increase of *da/dN* with GTN, for all values of ΔK studied.
- There is a global trend for the increase of porosity with plastic strain. An oscillatory behaviour is observed in each load cycle because the stress verified at the crack tip is of compressive nature during the unloading phase. This causes the micro voids on the material to partially close. The increase of crack length, and therefore of ΔK, also increases the porosity level.
- The variation of porosity with plastic strain is relatively complex. This complexity was explained by the strong link found between stress triaxiality and porosity level.
- The inclusion of the nucleation process naturally induces higher fatigue crack growth rates, while some saturation occurs on crack closure.

- The sensitivity analysis showed that the parameter q_2, introduced by Tvergaard to account for the effect of stress tri-axiality, which tends to be high at a crack tip, is the most relevant parameter concerning crack growth rates.
- The nucleation amplitude, f_N, and q_1, another parameter introduced by Tvergaard to account for the loss of strength due to inter-void interactions, are of secondary importance. Finally, da/dN showed to have almost null sensitivity to q_3.

7. SUGESTIONS FOR FUTURE WORK

In continuity to this work, it would be interesting to study the following issues:

- In a previous work, the numerical predictions based on cyclic plastic deformation underestimated the effect of stress ratio. The inclusion of the GTN, analogously to what was presented in this study, is expected to enhance the influence of the stress ratio. Besides, it is important to check if, in the absence of crack closure, the model still verifies no effect of stress ratio. This will allow to find if there is an effect of $K_{\max}$ on FCG as it is claimed by several authors.
- Apply the numerical model used in this study to variable amplitude loading cases, namely on the application of single overloads to the 6082-T6 aluminium alloy. The GTN is expected to increase the crack increment affected by the overload, as the initial numerical prediction (i.e. without GTN) underestimate the influence of the overloads in comparison with experimental results [40].
- Apply this model to the study ductile failure in the 18Ni300 maraging steel and compare the results with the ones attained experimentally by a brazilian partner. The study of ductile failure is of interest to understand regime III of da/dN-ΔK curves.
- Finally, it would be interesting to study environmental damage, which is relevant particularly relevant at low ΔK values, near threshold, and at elevated temperature. The inclusion of this relevant mechanism on the analysis of FCG is of major importance.

BIBLIOGRAPHY

[1] CAMPBELL, J., “Invisible macrodefects in castings,” *J. Phys. IV Fr.*, vol. 03, pp. C7-861-C7-872, 1993, doi: 10.1051/jp4:19937135.

[2] H. Masuo *et al.*, “Influence of defects, surface roughness and HIP on the fatigue strength of Ti-6Al-4V manufactured by additive manufacturing,” *Int. J. Fatigue*, vol. 117, pp. 163–179, 2018, doi: https://doi.org/10.1016/j.ijfatigue.2018.07.020.

[3] C. Bathias and A. Pineau, *Fatigue of Materials and Structures: Application to Damage and Design*. 2013.

[4] F. Erdogan and M. Ratwani, “Fatigue and fracture of cylindrical shells containing a circumferential crack,” *Int. J. Fract. Mech.*, vol. 6, no. 4, pp. 379–392, 1970, doi: 10.1007/BF00182626.

[5] P. Paris and F. Erdogan, “A critical analysis of crack propagation laws,” *J. Basic Eng., Trans. ASME*, vol. 85, no. 4, pp. 528–533, Dec. 1963, doi: 10.1115/1.3656900.

[6] A. Hartman and J. Schijve, “The effects of environment and load frequency on the crack propagation law for macro fatigue crack growth in aluminium alloys,” *Eng. Fract. Mech.*, vol. 1, no. 4, pp. 615–631, 1970, doi: https://doi.org/10.1016/0013-7944(70)90003-2.

[7] B. Marques, M. F. Borges, F. V Antunes, J. M. Vasco-Olmo, F. A. Díaz, and M. N. James, “Limitations of small-scale yielding for fatigue crack growth,” *Eng. Fract. Mech.*, vol. 252, p. 107806, 2021, doi: https://doi.org/10.1016/j.engfracmech.2021.107806.

[8] M. F. Borges, “Effect of elasto-plastic properties on fatigue crack growth.” Universidade de Coimbra, 2019.

[9] H. Chen, W. Chen, T. Li, and J. Ure, “Effect of circular holes on the ratchet limit and crack tip plastic strain range in a centre cracked plate,” *Eng. Fract. Mech.*, vol. 78, no. 11, pp. 2310–2324, 2011, doi: https://doi.org/10.1016/j.engfracmech.2011.05.004.

[10] H.-B. Park, K.-M. Kim, and B.-W. Lee, “Plastic zone size in fatigue cracking,” *Int. J. Press. Vessel. Pip.*, vol. 68, no. 3, pp. 279–285, 1996, doi: https://doi.org/10.1016/0308-0161(95)00066-6.

[11] P. K. Liaw, S. I. Kwun, and M. E. Fine, “Plastic work of fatigue crack propagation in steels and aluminum alloys,” *Metall. Trans. A*, vol. 12, no. 1, pp. 49–55, 1981, doi: 10.1007/BF02648507.

[12] V. Tvergaard, “On fatigue crack growth in ductile materials by crack–tip blunting,” *J. Mech. Phys. Solids*, vol. 52, no. 9, pp. 2149–2166, 2004, doi: https://doi.org/10.1016/j.jmps.2004.02.007.

[13] R. Pippan and W. Grosinger, “Fatigue crack closure: From LCF to small scale yielding,” *Int. J. Fatigue*, vol. 46, pp. 41–48, 2013, doi: https://doi.org/10.1016/j.ijfatigue.2012.02.016.

[14] F. V Antunes, R. Branco, P. A. Prates, and L. Borrego, “Fatigue crack growth modelling based on CTOD for the 7050-T6 alloy,” *Fatigue Fract. Eng. Mater. Struct.*, vol. 40, no. 8, pp. 1309–1320, 2017, doi: https://doi.org/10.1111/ffe.12582.

[15] J. M. Vasco-Olmo, F. A. Díaz, F. V Antunes, and M. N. James, “Characterisation of

fatigue crack growth using digital image correlation measurements of plastic CTOD," *Theor. Appl. Fract. Mech.*, vol. 101, pp. 332–341, 2019, doi: https://doi.org/10.1016/j.tafmec.2019.03.009.
[16] R. Hamam, S. Pommier, and F. Bumbieler, "Mode I fatigue crack growth under biaxial loading," *Int. J. Fatigue*, vol. 27, no. 10, pp. 1342–1346, 2005, doi: https://doi.org/10.1016/j.ijfatigue.2005.06.020.
[17] M. Borges, D. M. Neto, and F. V Antunes, "Numerical simulation of fatigue crack growth based on accumulated plastic strain," *Theor. Appl. Fract. Mech.*, vol. 108, p. 102676, 2020, doi: 10.1016/j.tafmec.2020.102676.
[18] Z. S. Hosseini, M. Dadfarnia, B. P. Somerday, P. Sofronis, and R. O. Ritchie, "On the theoretical modeling of fatigue crack growth," *J. Mech. Phys. Solids*, vol. 121, pp. 341–362, 2018, doi: https://doi.org/10.1016/j.jmps.2018.07.026.
[19] Y. Jiang and M. Feng, "Modeling of Fatigue Crack Propagation," *J. Eng. Mater. Technol. Asme - J ENG MATER TECHNOL*, vol. 126, 2004, doi: 10.1115/1.1631026.
[20] D. M. Neto, M. F. Borges, F. V Antunes, and J. Jesus, "Mechanisms of fatigue crack growth in Ti-6Al-4V alloy subjected to single overloads," *Theor. Appl. Fract. Mech.*, vol. 114, p. 103024, 2021, doi: https://doi.org/10.1016/j.tafmec.2021.103024.
[21] F. F. Ferreira, D. M. Neto, J. S. Jesus, P. A. Prates, and F. V Antunes, "Numerical Prediction of the Fatigue Crack Growth Rate in SLM Ti-6Al-4V Based on Crack Tip Plastic Strain," *Metals (Basel).*, vol. 10, no. 9, 2020, doi: 10.3390/met10091133.
[22] X. F. Chen, C. L. Chow, and B. J. Duggan, "A DUCTILE DAMAGE MODEL BASED ON ENDOCHRONIC PLASTIC THEORY AND ITS APPLICATION IN FAILURE ANALYSIS," in *Advances in Engineering Plasticity and its Applications*, W. B. LEE, Ed. Oxford: Elsevier, 1993, pp. 333–340.
[23] F. Rahimidehgolan, G. Majzoobi, F. Alinejad, and J. F. Sola, "Determination of the constants of GTN damage model using experiment, polynomial regression and kriging methods," *Appl. Sci.*, vol. 7, no. 11, 2017, doi: 10.3390/app7111179.
[24] Y. Wei, C. L. Chow, and B. J. Duggan, "A DAMAGE MODEL OF FATIGUE ANALYSIS FOR AL ALLOY 2024-T3," in *Advances in Engineering Plasticity and its Applications*, W. B. LEE, Ed. Oxford: Elsevier, 1993, pp. 325–332.
[25] J. Lemaitre, "Phenomenological Aspects of Damage," in *A Course on Damage Mechanics*, Berlin, Heidelberg: Springer Berlin Heidelberg, 1996, pp. 1–37.
[26] C. A. G. de M. Branco, *Mecânica dos materiais*. Lisboa: Fundação Calouste Gulbenkian, 2011.
[27] "Fracture processes of aerospace materials," in *Introduction to Aerospace Materials*, Elsevier, 2012, pp. 428–453.
[28] A. A. Griffith, "Philosophical transactions of the royal society of london," *Ser. A, Contain. Pap. a Math. or Phys. character*, vol. 221, pp. 163–198, 1921.
[29] G. R. Irwin, "Fracturing of metals," *ASM, Clevel.*, vol. 147, p. 19, 1948.
[30] G. R. Irwin, "Analysis of stresses and strains near the end of a crack traversing a plate," vol. 24, pp. 361–364, 1957.
[31] J. Rice, "Mechanics of Crack Tip Deformation and Extension by Fatigue," *Mech. Crack Tip Deform. Ext. by Fatigue*, vol. 415, pp. 247–309, 1967.
[32] J. C. Newman and I. S. Raju, "An empirical stress-intensity factor equation for the surface crack," *Eng. Fract. Mech.*, vol. 15, no. 1, pp. 185–192, 1981, doi: https://doi.org/10.1016/0013-7944(81)90116-8.

[33] P. C. Paris, M. P. Gomez, and W. E. Anderson, “A rational analytic theory of fatigue,” in *The Trend in Engineering 13*, 1961, pp. 9–14.

[34] C. T. Sun and Z.-H. Jin, “Chapter 7 - Elastic-Plastic Fracture Criteria,” C. T. Sun and Z.-H. B. T.-F. M. Jin, Eds. Boston: Academic Press, 2012, pp. 171–187.

[35] F. V Antunes, S. Serrano, R. Branco, and P. Prates, “Fatigue crack growth in the 2050-T8 aluminium alloy,” *Int. J. Fatigue*, vol. 115, pp. 79–88, 2018, doi: https://doi.org/10.1016/j.ijfatigue.2018.03.020.

[36] R. H. Christensen, “Fatigue crack growth affected by metal fragments wedged between opening-closing crack surfaces,” *Appl Mater Res*, vol. 2, no. 4, pp. 207–210, 1963.

[37] E. Wolf, “Fatigue crack closure under cyclic tension,” *Eng. Fract. Mech.*, vol. 2, no. 1, pp. 37–45, 1970, doi: https://doi.org/10.1016/0013-7944(70)90028-7.

[38] W. Elber, “The Significance of Fatigue Crack Closure,” in *Damage Tolerance in Aircraft Structures*, M. S. Rosenfeld, Ed. West Conshohocken, PA: ASTM International, 1971, pp. 230–242.

[39] L. P. Borrego, J. M. Ferreira, and J. M. Costa, “Fatigue crack growth and crack closure in an AlMgSi alloy,” *Fatigue Fract. Eng. Mater. Struct.*, vol. 24, no. 4, pp. 255–265, 2001, doi: https://doi.org/10.1046/j.1460-2695.2001.00383.x.

[40] L. P. Borrego, J. M. Ferreira, J. M. Pinho da Cruz, and J. M. Costa, “Evaluation of overload effects on fatigue crack growth and closure,” *Eng. Fract. Mech.*, vol. 70, no. 11, pp. 1379–1397, 2003, doi: https://doi.org/10.1016/S0013-7944(02)00119-4.

[41] K. T. V. Rao, W. Yu, and R. O. Ritchie, “On the behavior of small fatigue cracks in commercial aluminum-lithium alloys,” *Eng. Fract. Mech.*, vol. 31, no. 4, pp. 623–635, 1988, doi: https://doi.org/10.1016/0013-7944(88)90105-1.

[42] J. D. M. Costa and J. A. M. Ferreira, “Effect of stress ratio and specimen thickness on fatigue crack growth of CK45 steel,” *Theor. Appl. Fract. Mech.*, vol. 30, no. 1, pp. 65–73, 1998, doi: https://doi.org/10.1016/S0167-8442(98)00044-5.

[43] R. O. Ritchie, “SLOW CRACK GROWTH: MACROSCOPIC AND MICROSCOPIC ASPECTS,” in *Fracture and Fracture Mechanics*, R. B. TAIT and G. G. GARRETT, Eds. Pergamon, 1985, pp. 93–124.

[44] S. Suresh, G. F. Zamiski, and D. R. O. Ritchie, “Oxide-Induced Crack Closure: An Explanation for Near-Threshold Corrosion Fatigue Crack Growth Behavior,” *Metall. Mater. Trans. A*, vol. 12, no. 8, pp. 1435–1443, 1981, doi: 10.1007/BF02643688.

[45] G. T. Gray, J. C. Williams, and A. W. Thompson, “Roughness-Induced Crack Closure: An Explanation for Microstructurally Sensitive Fatigue Crack Growth,” *Metall. Trans. A*, vol. 14, no. 2, pp. 421–433, 1983, doi: 10.1007/BF02644220.

[46] S. K. Paul and S. Tarafder, “Cyclic plastic deformation response at fatigue crack tips,” *Int. J. Press. Vessel. Pip.*, vol. 101, pp. 81–90, 2013, doi: https://doi.org/10.1016/j.ijpvp.2012.10.007.

[47] F. V Antunes, R. Branco, L. Correia, and A. Ramalho, “A numerical study of non-linear crack tip parameters,” *Frat. ed Integrita Strutt.*, vol. 9, pp. 199–208, 2015, doi: 10.3221/IGF-ESIS.33.25.

[48] F. V Antunes and D. M. Rodrigues, “Numerical simulation of plasticity induced crack closure: Identification and discussion of parameters,” *Eng. Fract. Mech.*, vol. 75, no. 10, pp. 3101–3120, 2008, doi: https://doi.org/10.1016/j.engfracmech.2007.12.009.

[49] A. A. Wells, “Unstable crack propagation in metals: cleavage and fast fracture,” in

Proceedings of the crack propagation symposium, 1961, vol. 1, no. 84.

[50] C. Laird and G. C. Smith, "Initial stages of damage in high stress fatigue in some pure metals," *Philos. Mag. A J. Theor. Exp. Appl. Phys.*, vol. 8, no. 95, pp. 1945–1963, 1963, doi: 10.1080/14786436308209084.

[51] R. M. N. Pelloux, "Crack extension by alternating shear," *Eng. Fract. Mech.*, vol. 1, no. 4, pp. 697–704, 1970, doi: https://doi.org/10.1016/0013-7944(70)90008-1.

[52] D. J. Nicholls, "THE RELATION BETWEEN CRACK BLUNTING AND FATIGUE CRACK GROWTH RATES," *Fatigue Fract. Eng. Mater. Struct.*, vol. 17, no. 4, pp. 459–467, 1994, doi: https://doi.org/10.1111/j.1460-2695.1994.tb00245.x.

[53] F. V Antunes, S. M. Rodrigues, R. Branco, and D. Camas, "A numerical analysis of CTOD in constant amplitude fatigue crack growth," *Theor. Appl. Fract. Mech.*, vol. 85, pp. 45–55, 2016, doi: https://doi.org/10.1016/j.tafmec.2016.08.015.

[54] F. V Antunes, M. S. C. Ferreira, R. Branco, P. Prates, C. Gardin, and C. Sarrazin-Baudoux, "Fatigue crack growth versus plastic CTOD in the 304L stainless steel," *Eng. Fract. Mech.*, vol. 214, pp. 487–503, 2019, doi: https://doi.org/10.1016/j.engfracmech.2019.04.013.

[55] J. C. Newman, "A Finite-Element Analysis of Fatigue Crack Closure," in *Mechanics of Crack Growth*, J. R. Rice and P. C. Paris, Eds. West Conshohocken, PA: ASTM International, 1976, pp. 281–301.

[56] J. Pokluda, "Dislocation-based model of plasticity and roughness-induced crack closure," *Int. J. Fatigue*, vol. 46, pp. 35–40, 2013, doi: https://doi.org/10.1016/j.ijfatigue.2011.11.016.

[57] J. S. Jesus, L. P. Borrego, J. A. M. Ferreira, J. D. Costa, and C. Capela, "Fatigue crack growth behaviour in Ti6Al4V alloy specimens produced by selective laser melting," *Int. J. Fract.*, vol. 223, no. 1, pp. 123–133, 2020, doi: 10.1007/s10704-019-00417-2.

[58] R. Sunder, "Unraveling the Science of Variable Amplitude Fatigue ," *J. ASTM Int.*, vol. 9, no. 1, pp. 1–32, Dec. 2011, doi: 10.1520/JAI103940.

[59] R. Pippan, C. BICHLER, B. TABERNIG, and H. WEINHANDL, "Overloads in ductile and brittle materials," *Fatigue Fract. Eng. Mater. Struct.*, vol. 28, pp. 971–981, 2005, doi: 10.1111/j.1460-2695.2005.00934.x.

[60] J. A. Newman, S. W. Smith, and R. S. Piascik, "Kmax effects on the near-threshold fatigue crack growth of powder-metallurgy aluminum alloys," *Int. J. Fatigue*, vol. 31, no. 8, pp. 1237–1245, 2009, doi: https://doi.org/10.1016/j.ijfatigue.2009.01.002.

[61] M. F. Borges, D. M. Neto, and F. V Antunes, "Revisiting Classical Issues of Fatigue Crack Growth Using a Non-Linear Approach.," *Mater. (Basel, Switzerland)*, vol. 13, no. 23, Dec. 2020, doi: 10.3390/ma13235544.

[62] G. Rousselier, "Ductile fracture models and their potential in local approach of fracture," *Nucl. Eng. Des.*, vol. 105, no. 1, pp. 97–111, 1987, doi: https://doi.org/10.1016/0029-5493(87)90234-2.

[63] T. C. F., "No Title," *Metallurgia*, vol. 39, p. 133, 1948.

[64] K. E. Puttick, "Ductile fracture in metals," *Philos. Mag. A J. Theor. Exp. Appl. Phys.*, vol. 4, no. 44, pp. 964–969, 1959, doi: 10.1080/14786435908238272.

[65] F. A. McClintock, "A Criterion for Ductile Fracture by the Growth of Holes," *J. Appl. Mech.*, vol. 35, no. 2, pp. 363–371, Jun. 1968, doi: 10.1115/1.3601204.

[66] W. M. Garrison and N. R. Moody, "Ductile fracture," *J. Phys. Chem. Solids*, vol. 48, no. 11, pp. 1035–1074, 1987, doi: https://doi.org/10.1016/0022-3697(87)90118-1.

[67] J. R. Rice and D. M. Tracey, “On the ductile enlargement of voids in triaxial stress fields∗,” *J. Mech. Phys. Solids*, vol. 17, no. 3, pp. 201–217, 1969, doi: https://doi.org/10.1016/0022-5096(69)90033-7.

[68] Y. Bao, “Prediction of ductile crack formation in uncracked bodies,” 2003.

[69] T. L. Anderson, “Fracture mechanics : fundamentals and applications.” pp. 73–74, 2005, [Online]. Available: http://site.ebrary.com/id/11166314.

[70] J. Besson, “Continuum Models of Ductile Fracture: A Review,” *Int. J. Damage Mech.*, vol. 19, no. 1, pp. 3–52, 2010, doi: 10.1177/1056789509103482.

[71] A. H. Cottrell, “Mechanics of Fracture in Large Structures,” *Proc. R. Soc. Lond. A. Math. Phys. Sci.*, vol. 285, no. 1400, pp. 10–21, Mar. 1965, [Online]. Available: http://www.jstor.org/stable/2415085.

[72] J. Brito, “Ductile fracture prediction using a coupled damage model,” 2018.

[73] J.-J. Marigo, C. Maurini, and K. Pham, “An overview of the modelling of fracture by gradient damage models,” *Meccanica*, vol. 51, no. 12, pp. 3107–3128, 2016, doi: 10.1007/s11012-016-0538-4.

[74] J. Lemaitre and J. Dufailly, “Damage measurements,” *Eng. Fract. Mech.*, vol. 28, no. 5, pp. 643–661, 1987, doi: https://doi.org/10.1016/0013-7944(87)90059-2.

[75] R. Kiran and K. Khandelwal, “Gurson model parameters for ductile fracture simulation in ASTM A992 steels,” *Fatigue Fract. Eng. Mater. Struct.*, vol. 37, no. 2, pp. 171–183, 2014, doi: https://doi.org/10.1111/ffe.12097.

[76] L. Xue, “Ductile fracture modeling: Theory, experimental investigation and numerical verification,” *Massachusetts Inst. Technol.*, 2009.

[77] J. Lemaitre, “A CONTINUOUS DAMAGE MECHANICS MODEL FOR DUCTILE FRACTURE,” *J. Eng. Mater. Technol. Asme*, vol. 107, pp. 83–89, 1985.

[78] M. Brünig, S. Gerke, and V. Hagenbrock, “Micro-mechanical studies on the effect of the stress triaxiality and the Lode parameter on ductile damage,” *Int. J. Plast.*, vol. 50, pp. 49–65, 2013, doi: https://doi.org/10.1016/j.ijplas.2013.03.012.

[79] J. L. Alves, B. Revil-Baudard, and O. Cazacu, “Importance of the coupling between the sign of the mean stress and the third invariant on the rate of void growth and collapse in porous solids with a von Mises matrix,” *Model. Simul. Mater. Sci. Eng.*, vol. 22, no. 2, p. 25005, Jan. 2014, doi: 10.1088/0965-0393/22/2/025005.

[80] J. B. Stewart, “Development of Yield Criteria for Describing the Behavior of,” pp. 1–251, 2009.

[81] T. Pardoen and J. W. Hutchinson, “An extended model for void growth and coalescence,” *J. Mech. Phys. Solids*, vol. 48, no. 12, pp. 2467–2512, 2000, doi: https://doi.org/10.1016/S0022-5096(00)00019-3.

[82] A. L. Gurson, “Continuum Theory of Ductile Rupture by Void Nucleation and Growth: Part I—Yield Criteria and Flow Rules for Porous Ductile Media,” *J. Eng. Mater. Technol.*, vol. 99, no. 1, pp. 2–15, Jan. 1977, doi: 10.1115/1.3443401.

[83] J. L. Chaboche, M. Boudifa, and K. Saanouni, “A CDM approach of ductile damage with plastic compressibility,” *Int. J. Fract.*, vol. 137, no. 1–4, pp. 51–75, 2006, doi: 10.1007/s10704-005-3061-5.

[84] L. Malcher, “Continuum Modelling and Numerical Simulation of Damage for Ductile Materials,” *Fac. Eng. Univ. do Porto*, 2012, doi: 10.13140/RG.2.2.33392.81926.

[85] V. Tvergaard, “Influence of voids on shear band instabilities under plane strain conditions,” *Int. J. Fract.*, vol. 17, no. 4, pp. 389–407, 1981, doi: 10.1007/BF00036191.

[86] V. Tvergaard, “On localization in ductile materials containing spherical voids,” *Int. J. Fract.*, vol. 18, no. 4, pp. 237–252, 1982, doi: 10.1007/BF00015686.

[87] K. L. Nielsen, “Predicting failure response of spot welded joints using recent extensions to the Gurson model,” *Comput. Mater. Sci.*, vol. 48, no. 1, pp. 71–82, 2010, doi: 10.1016/j.commatsci.2009.12.004.

[88] C. C. Chu and A. Needleman, “Void Nucleation Effects in Biaxially Stretched Sheets,” *J. Eng. Mater. Technol.*, vol. 102, no. 3, pp. 249–256, Jul. 1980, doi: 10.1115/1.3224807.

[89] V. Tvergaard and A. Needleman, “Analysis of the cup-cone fracture in a round tensile bar,” *Acta Metall.*, vol. 32, no. 1, pp. 157–169, 1984, doi: https://doi.org/10.1016/0001-6160(84)90213-X.

[90] A. Kami, B. M. Dariani, D. Com_a, D. Banabic, A. Vanini, and M. Liewald, “Calibration of GTN damage model parameters using hydraulic bulge test,” 2018.

[91] L. Ying, W. Liu, D. Wang, and P. Hu, “Parameter Calibration of GTN Damage Model and Formability Analysis of 22MnB5 in Hot Forming Process,” *J. Mater. Eng. Perform.*, vol. 26, no. 11, pp. 5155–5165, 2017, doi: 10.1007/s11665-017-2962-6.

[92] G. Shatil and L. Wang, “THE DEPENDENCY OF THE LOCAL APPROACH TO FRACTURE ON THE CALIBRATION OF MATERIAL PARAMETERS.”

[93] M. Springmann and M. Kuna, “Identification of material parameters of the Gurson-Tvergaard-Needleman model by combined experimental and numerical techniques,” *Comput. Mater. Sci.*, vol. 32, no. 3–4, pp. 544–552, 2005, doi: 10.1016/j.commatsci.2004.09.010.

[94] V. Kozák and V. Libor, “Parameters Identification for GTN Model and Their Verification on 42CrMo4 Steel,” in *Materials Structure & Micromechanics of Fracture*, 2005, vol. 482, pp. 335–338, doi: 10.4028/www.scientific.net/MSF.482.335.

[95] L. Malcher, F. J. P. Reis, F. M. Andrade Pires, and J. M. A. César de Sá, “Evaluation of shear mechanisms and influence of the calibration point on the numerical results of the GTN model,” *Int. J. Mech. Sci.*, vol. 75, pp. 407–422, 2013, doi: https://doi.org/10.1016/j.ijmecsci.2013.08.008.

[96] M. Feucht, D. Sun, T. Erhart, and T. Frank, “Recent development and applications of the Gurson model,” 2006.

[97] D. Chen, Y. Li, X. Yang, W. Jiang, and L. Guan, “Efficient parameters identification of a modified GTN model of ductile fracture using machine learning,” *Eng. Fract. Mech.*, vol. 245, p. 107535, 2021, doi: https://doi.org/10.1016/j.engfracmech.2021.107535.

[98] M. Abbasi, M. Ketabchi, H. Izadkhah, D. H. Fatmehsaria, and A. N. Aghbash, “Identification of GTN model parameters by application of response surface methodology,” *Procedia Eng.*, vol. 10, pp. 415–420, 2011, doi: https://doi.org/10.1016/j.proeng.2011.04.070.

[99] Y. X. Yan, Q. Sun, J. J. Chen, and H. L. Pan, “Analysis for the Propagation of Edge Crack of Silicon Steel during Cold Rolling Process Based on GTN Damage Model,” in *Advanced Composite Materials*, 2012, vol. 482, pp. 487–492, doi: 10.4028/www.scientific.net/AMR.482-484.487.

[100] S. Kweon, “Damage at negative triaxiality,” *Eur. J. Mech. - A/Solids*, vol. 31, no. 1, pp. 203–212, 2012, doi: https://doi.org/10.1016/j.euromechsol.2011.02.005.

[101] F. Abbassi, O. Pantalé, S. Mistou, A. Zghal, and R. Rakotomalala, “Effect of

Ductile Damage Evolution in Sheet Metal Forming: Experimental and Numerical Investigations," in *Structural Analysis of Advanced Materials*, 2010, vol. 446, pp. 157–169, doi: 10.4028/www.scientific.net/KEM.446.157.

[102] A. Kami, B. Dariani, S. ali sadough vanini, D.-S. Comsa, and D. Banabic, "Application of a GTN Damage Model to Predict the Fracture of Metallic Sheets Subjected to Deep-Drawing," *Proc. Rom. Acad. - Ser. A Math. Physics, Tech. Sci. Inf. Sci.*, vol. 15, pp. 300–309, Jul. 2014.

[103] R. S. Neves, G. V Ferreira, and L. Malcher, "Gurson-based incremental damage in fatigue life estimate under proportional and non-proportional loading: Constant amplitude and low cycle regime applications," *Theor. Appl. Fract. Mech.*, vol. 108, p. 102678, 2020, doi: https://doi.org/10.1016/j.tafmec.2020.102678.

[104] L. Ying, D. Wang, W. Liu, Y. Wu, and P. Hu, "On the numerical implementation of a shear modified GTN damage model and its application to small punch test," *Int. J. Mater. Form.*, vol. 11, no. 4, pp. 527–539, 2018, doi: 10.1007/s12289-017-1362-7.

[105] K. Nahshon and J. W. Hutchinson, "Modification of the Gurson Model for shear failure," *Eur. J. Mech. - A/Solids*, vol. 27, no. 1, pp. 1–17, 2008, doi: https://doi.org/10.1016/j.euromechsol.2007.08.002.

[106] L. Xue, "Constitutive modeling of void shearing effect in ductile fracture of porous materials," *Eng. Fract. Mech.*, vol. 75, no. 11, pp. 3343–3366, 2008, doi: https://doi.org/10.1016/j.engfracmech.2007.07.022.

[107] O. Cazacu and J. B. Stewart, "Analytic plastic potential for porous aggregates with matrix exhibiting tension–compression asymmetry," *J. Mech. Phys. Solids*, vol. 57, no. 2, pp. 325–341, 2009, doi: https://doi.org/10.1016/j.jmps.2008.10.010.

[108] L. F. Menezes and C. Teodosiu, "Three-dimensional numerical simulation of the deep-drawing process using solid finite elements," *J. Mater. Process. Technol.*, vol. 97, no. 1, pp. 100–106, 2000, doi: https://doi.org/10.1016/S0924-0136(99)00345-3.

[109] M. C. Oliveira, J. L. Alves, and L. F. Menezes, "Algorithms and Strategies for Treatment of Large Deformation Frictional Contact in the Numerical Simulation of Deep Drawing Process," *Arch. Comput. Methods Eng.*, vol. 15, no. 2, pp. 113–162, 2008, doi: 10.1007/s11831-008-9018-x.

[110] M. F. Borges, F. V Antunes, B. Moreno, P. Prates, D. Camas, and D. M. Neto, "Fatigue crack propagation analysis in 2024-T351 aluminium alloy using nonlinear parameters," *Int. J. Fatigue*, no. Apr, 2021.

[111] ASTM E 647-11: Standard test method for measurement of fatigue crack growth rates. Philadelphia: American Society for Testing and Materials, 2011, ASTM

[112] T. J. R. Hughes, "Generalization of selective integration procedures to anisotropic and nonlinear media," *Int. J. Numer. Methods Eng.*, vol. 15, no. 9, pp. 1413–1418, Sep. 1980, doi: https://doi.org/10.1002/nme.1620150914.

[113] F. V Antunes, D. Camas, L. Correia, and R. Branco, "Finite element meshes for optimal modelling of plasticity induced crack closure," *Eng. Fract. Mech.*, vol. 142, pp. 184–200, 2015, doi: https://doi.org/10.1016/j.engfracmech.2015.06.007.

[114] L. Zhao, J. Tong, and J. Byrne, "The evolution of the stress–strain fields near a fatigue crack tip and plasticity-induced crack closure revisited," *Fatigue Fract. Eng. Mater. Struct.*, vol. 27, pp. 19–29, 2004, doi: 10.1111/j.1460-2695.2004.00716.x.

[115] K. Vor, C. Gardin, C. Sarrazin-Baudoux, and J. Petit, "Wake length and loading history effects on crack closure of through-thickness long and short cracks in 304L: Part II – 3D numerical simulation," *Eng. Fract. Mech.*, vol. 99, pp. 306–323, 2013, doi: https://doi.org/10.1016/j.engfracmech.2013.01.014.

[116] D. M. Rodrigues and F. V Antunes, “Finite element simulation of plasticity induced crack closure with different material constitutive models,” *Eng. Fract. Mech.*, vol. 76, no. 9, pp. 1215–1230, 2009, doi: https://doi.org/10.1016/j.engfracmech.2009.01.014.

[117] B. Teng, W. Wang, and Y. Xu, “Ductile fracture prediction in aluminium alloy 5A06 sheet forming based on GTN damage model,” *Eng. Fract. Mech.*, vol. 186, pp. 242–254, 2017, doi: https://doi.org/10.1016/j.engfracmech.2017.10.014.